Dynamics of a polarized vortex ring

By D. VIRK[1], M. V. MELANDER[2] and F. HUSSAIN[1]

[1] Department of Mechanical Engineering, University of Houston, Houston, TX 77204–4792, USA

[2] Department of Mathematics, Southern Methodist University, Dallas, TX 75275, USA

This paper builds on our claim that most vortical structures in transitional and turbulent flows are partially polarized. Polarization is inferred by the application of helical wave decomposition. We analyse initially polarized isolated viscous vortex rings through direct numerical simulation of the Navier–Stokes equations using divergence-free axisymmetric eigenfunctions of the curl operator. Integral measures of the degree of polarization, such as the fractions of energy, enstrophy, and helicity associated with right-handed (or left-handed) eigenfunctions, remain nearly constant during evolution, thereby suggesting that polarization is a persistent feature. However, for polarized rings an axial vortex (tail) develops near the axis, where the local ratio of right- to left-handed vorticities develops significant non-uniformities due to spatial separation of peaks of polarized components. Reconnection can occur in rings when polarized and is clearly discerned from the evolution of axisymmetric vortex surfaces; but interestingly, the location of reconnection cannot be inferred from the vorticity magnitude. The ring propagation velocity U_p decreases monotonically as the degree of initial polarization increases. Unlike force-balance arguments, two explanations based on vortex dynamics provided here are not restricted to thin rings and predict reduction in U_p correctly. These results reveal surprising differences among the evolutionary dynamics of polarized, partially polarized, and unpolarized rings.

1. Introduction

Vortex rings without swirl (i.e. azimuthal flow) have been studied extensively, but little is known about vortex rings with swirl. This latter flow is of interest since we believe it can help us understand axisymmetric vortex breakdown, as also noted by Shariff & Leonard (1992), and has distributed vorticity with non-zero helicity (Moffatt 1969). However, starting with the pioneering work of Hicks (1899), research on rings with swirl has mostly been limited to obtaining steady solutions of the Euler equations (Moffatt 1988; Turkington 1989), except for some recent simulations specifically designed to address the question of a possible finite-time singularity in the Euler equations (Grauer & Sideris 1991; Pumir & Siggia 1992*a,b*). Our focus is on the *dynamics* of rings with helical vortex lines.

In order to define polarization and understand its relevance to turbulent flows, it is necessary to consider the generalized Helmholtz theorem given by Moses (1971) or the equivalent complex Helical Wave Decomposition (HWD) of Lesieur (1990), which allows decomposition of a three-dimensional vector field into three components: potential part, 'left-handed', and 'right-handed'. The last two are unique, Galilean invariant and their sum equals the solenoidal part of the vector field. HWD is based on eigenfunctions of the curl operator, such that the right-handed component is a superposition of eigenmodes with positive eigenvalues, while the left-handed component is a linear combination of eigenmodes with negative eigenvalues. The two

classes of eigenmodes differ in the helical twist of the vector lines (e.g. vortex lines). In the one with negative eigenvalues, the vector lines are left-handed helices, and in the other they are right-handed helices – hence their names. Equivalently, we also refer to these components as left or right *polarized*. In a vorticity field free of helically twisted vortex lines, the two polarized components are everywhere equal in magnitude. We have used HWD to analyse flow fields obtained via three-dimensional direct numerical simulations, such as circular jets (Melander, Hussain & Basu 1991). These analyses strongly suggest that partially polarized structures are a common feature in most transitional and turbulent flows, and that they are generated during transition to turbulence. We view such polarized vortical structures as essential building blocks of turbulent flows. A study of the evolution and dynamics of helical vortical structures is therefore an obvious avenue for understanding three-dimensional vortical flows and their modelling. Poor understanding of the dynamics of both fully and partially polarized vortical structures suggests a detailed study of *isolated* polarized structures before interactions of such structures can be addressed.

One of the simplest isolated polarized structures with non-trivial evolution is an axisymmetric ring with swirl, which can be easily produced in a laboratory for experimental verification of analytical and numerical results. Contrary to Widnall, Bliss & Zalay's (1971) assertion, such rings may occur naturally as coherent structures in circular jets with small swirl. Note that polarized rings are a subclass of rings with swirl. Although polarized rings always have swirl (see figure 1 *a*), *vortex rings with swirl are not necessarily polarized*. Two examples to illustrate this point are shown in figure 1 (*b, c*). In the first, the axial vortex induces azimuthal flow inside the ring, but the ring is not polarized because the vortex lines are circular and not helical. In the second, a toroidal vorticity sheath induces swirl in the ring, yet the ring has circular vortex lines.

Axisymmetric rings are an optimum choice for capturing general three-dimensional features, as they allow easy interpretations. Unlike two-dimensional (Cartesian) flows, where the vortex lines extend to infinity, vortex lines in rings are confined to a compact region. Such vorticity distributions imply finite linear and angular impulses and their conservation, finite energy, and vanishing circulation in any plane cutting across the entire flow – as is the case in fully three-dimensional flows. In the absence of polarization, all vortex lines are circular and vortex stretching is proportional to the change in the circumference of a circular vortex line as it approaches or moves away from the symmetry axis. However, if the ring is polarized, coupling of swirl and meridional flow also causes reorientation of vortex lines, hence additional stretching. Another major advantage of axisymmetric flows with swirl is that one family of surfaces can be easily extracted, namely the axisymmetric vortex surfaces. This is in contrast to general three-dimensional flows, where computational determination of vortex surfaces is difficult, if not practically impossible. In addition, viscous axisymmetric flows with swirl allow changes in vortex line topology and the generation of total helicity.

Extensive literature on the dynamics of unpolarized rings already exists and can be readily used for comparison to analyse the effects of polarization. Even though the dynamics of a ring with swirl have not been studied in the past, effects of axial flow on the evolution of curved vortex filaments (Saffman 1970; Widnall *et al.* 1971; Moore & Saffman 1972) provide an important implication, namely that the propagation velocity U_p of a ring with swirl should be lower than that without swirl. These works have put forward an explanation (see §6) based on force-balance equations derived for thin rings. We present two vortex-dynamics-based explanations for U_p reduction which are valid for all rings. In this way, we address Shariff & Leonard's (1992) claim that Hill's
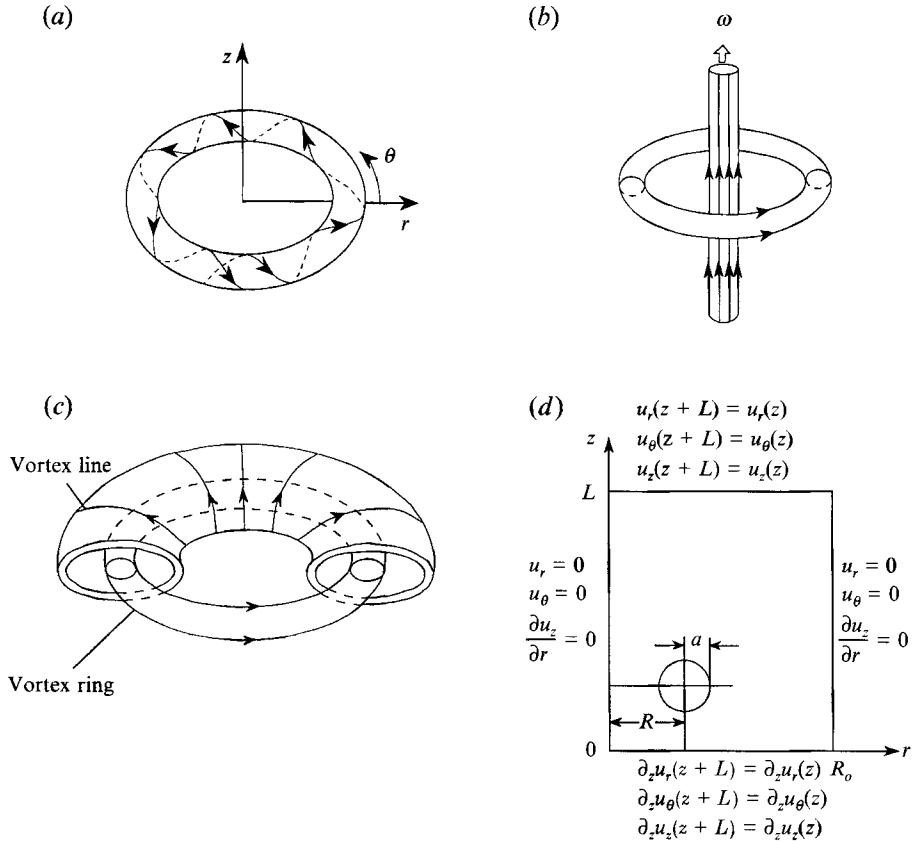
(a)

(b)

(c)

(d)

$$u_r(z + L) = u_r(z)$$
$$u_\theta(z + L) = u_\theta(z)$$
$$u_z(z + L) = u_z(z)$$

Vortex line

L

$u_r = 0$
$u_\theta = 0$
$\dfrac{\partial u_z}{\partial r} = 0$

$u_r = 0$
$u_\theta = 0$
$\dfrac{\partial u_z}{\partial r} = 0$

Vortex ring

$$\partial_z u_r(z + L) = \partial_z u_r(z) \quad R_o$$
$$\partial_z u_\theta(z + L) = \partial_z u_\theta(z)$$
$$\partial_z u_z(z + L) = \partial_z u_z(z)$$

FIGURE 1. (*a*) A schematic of the coordinate system and a typical vortex line on a right-handed polarized vortex ring. Note that the vortex line does not close after one revolution around the symmetry axis. This is typical behaviour. (*b*) Vortex ring around an axial vortex has swirl but it is *unpolarized*: i.e. the vortex lines in the ring are circular and not helical. (*c*) Vortex ring surrounded by toroidal vorticity sheath also has swirl, but it is unpolarized. (*d*) Boundary conditions for the derivation of the eigenfunctions of the curl operator in axisymmetric geometry. Radial extent of the domain is R_o and axial extent is L. The circle represents the cross-section of a vortex ring with ring radius R and core radius a.

spherical vortex with swirl (a decidedly thick ring) would actually move faster for weak swirl than without swirl. We find this claim to be contrary to our results and show analytically that such rings also move slower than their swirl-free counterparts. Other important issues addressed are the effects of polarization on the circulation decay, and whether the *degree of polarization* (defined later) changes significantly during evolution. Also studied are the striking features of the head–tail in a polarized ring, and the possible radially outward motion of the head (due to centrifugal force associated with swirl) during the entrainment and diffusion phase (Shariff & Leonard). We find that polarized ring dynamics differ significantly from the customary vorticity dynamics and include many new subtle and illuminating hydrodynamic effects of direct relevance to turbulent shear flows. One such effect is vortex reconnection within an isolated ring.

We have constructed an axisymmetric code based on HWD (§2) to simulate polarized rings. We use this code in other studies as well, but give all the details here for future reference. This code was validated by quantitative comparison with many published results obtained by different numerical methods. After discussing the

coupling between meridional flow and swirl in §3, and the polarized equations in §4, the evolution of polarized rings is analysed and compared to unpolarized rings in §5. Data on U_p and explanations for its reduction by swirl are presented in §6. Finally, key results are summarized in §7.

2. Numerical algorithm and initial conditions

2.1. *Basis functions*

An eigenfunction vector ($V \equiv V_r e_r + V_\theta e_\theta + V_z e_z$, where e_r, e_θ and e_z are unit vectors in the radial, azimuthal and axial directions, respectively) of the curl operator satisfies

$$\nabla \times V = \lambda V, \tag{1}$$

where $\lambda \in R$ is the eigenvalue. Taking the curl of (1) and assuming that V is divergence-free, we obtain

$$-\nabla^2 V = \lambda^2 V. \tag{2}$$

Substituting

$$V_r = R_r(r) Z_r(z), \quad V_\theta = R_\theta(r) Z_\theta(z), \quad V_z = R_z(r) Z_z(z)$$

into (2) we obtain

$$\frac{1}{R_r}\left(R_r'' + \frac{R_r'}{r} - \frac{R_r}{r^2}\right) + \lambda^2 = k^2, \quad \frac{-Z_r''}{Z_r} = k^2,$$

$$\frac{1}{R_\theta}\left(R_\theta'' + \frac{R_\theta'}{r} - \frac{R_\theta}{r^2}\right) + \lambda^2 = k^2, \quad \frac{-Z_\theta''}{Z_\theta} = k^2,$$

$$\frac{1}{R_z}\left(R_z'' + \frac{R_z'}{r}\right) + \lambda^2 = k^2, \quad \frac{-Z_z''}{Z_z} = k^2,$$

where (k^2) is the separation constant. Each of the above equations is a Sturm–Liouville problem and thus has real eigenvalues and orthogonal eigenfunctions, which form a complete set for square integrable functions in an unbounded domain. Imposing the boundary conditions shown in figure 1(*d*), the components of V are

$$V_r = AJ_1(q_j r)\,e^{ikz}, \quad V_\theta = BJ_1(q_j r)\,e^{ikz}, \quad V_z = CJ_0(q_j r)\,e^{ikz}, \tag{3a–c}$$

where J_1 and J_0 are Bessel functions of the first kind, k is the axial wavenumber, and

$$q_j = (\lambda_{j,k}^2 - k^2)^{\frac{1}{2}} = \beta_j/R_o; \quad \text{i.e.} \quad \lambda_{j,k} = \pm[(\beta_j/R_o)^2 + k^2]^{\frac{1}{2}},$$

where β_j (for $j = 1, 2, ..., N$) are zeros of J_1, $k = 2\pi l/L$ (for $l = 1, 2, ..., M$), R_o is the outer radius of the axisymmetric region being considered, and L is its axial extent. Here N and M are the numbers of radial and axial modes retained in our numerical simulations. Since (3*a–c*) are complex, the velocity and vorticity fields are made real by employing conjugate symmetry, e.g. $A(-k) = A^*(k)$, where ( )* denotes complex conjugation.

By imposing (1), we obtain for $k \neq 0$, $B = (i\lambda_{j,k}/k)A$ and $C = (iq_j/k)A$. The axisymmetric eigenfunctions of the curl operator can then be written as

$$V(r, z, \lambda_{j,k}) \equiv V_{j,k}^+ = \left(J_1(q_j r)\,e_r + \frac{i\lambda_{j,k}}{k}J_1(q_j r)\,e_\theta + \frac{iq_j}{k}J_0(q_j r)\,e_z\right)e^{ikz}, \tag{4a}$$

$$V(r, z, -\lambda_{j,k}) \equiv V_{j,k}^- = \left(J_1(q_j r)\,e_r - \frac{i\lambda_{j,k}}{k}J_1(q_j r)\,e_\theta + \frac{iq_j}{k}J_0(q_j r)\,e_z\right)e^{ikz}, \tag{4b}$$

where superscripts $+$ or $-$ denote the sign of $\lambda_{j,k}$. It is easily verified that

$$\nabla \times V_{j,k}^+ = \lambda_{j,k}\, V_{j,k}^+ \quad \text{and} \quad \nabla \times V_{j,k}^- = -\lambda_{j,k}\, V_{j,k}^-.$$

For $k = 0$, eigenfunctions can be derived similarly as

$$V_{j,0}^+ = J_1(q_j r)\,e_\theta + J_0(q_j r)\,e_z, \quad V_{j,0}^- = -J_1(q_j r)\,e_\theta + J_0(q_j r)\,e_z. \qquad (4c,d)$$

We call the eigenfunctions corresponding to negative eigenvalues ($\lambda_{j,k} < 0$) *left-handed* (denoted by subscript L) and those corresponding to positive eigenvalues ($\lambda_{j,k} > 0$) *right-handed* (denoted by subscript R). These eigenfunctions represent Beltrami flows and are exact solutions of the Euler equations.

2.2. *Algorithm to solve the Navier–Stokes equations using eigenfunctions of the curl operator*

In a rotating reference frame, the vorticity transport equation can be expressed as

$$\frac{\partial \omega}{\partial t} = \nabla \times (u \times (\omega + 2\Omega e_z)) - \nu\nabla \times (\nabla \times \omega), \qquad (5)$$

where Ω is the rotational velocity of the frame ($\Omega = 0$ in this study, but is implemented for generality in order to include configurations such as axial vortices with the boundary condition $u_\theta(R_o, z) = 0$). The vorticity field transforms into Bessel–Fourier space as $\hat{\omega} = \hat{\omega}_r e_r + \hat{\omega}_\theta e_\theta + \hat{\omega}_z e_z$, where

$$\hat{\omega}_r(\beta_j, k, t) = \sum_{l=0}^{M} \left(\frac{2}{R_o^2 [J_2(\beta_j)]^2} \int_0^{R_o} \omega_r(r, z_l, t) J_1\left(\frac{\beta_j r}{R_o}\right) r\, dr \right) e^{\frac{i2\pi(k-1)z_l}{L}}, \qquad (6a)$$

$$\hat{\omega}_\theta(\beta_j, k, t) = \sum_{l=0}^{M} \left(\frac{2}{R_o^2 [J_2(\beta_j)]^2} \int_0^{R_o} \omega_\theta(r, z_l, t) J_1\left(\frac{\beta_j r}{R_o}\right) r\, dr \right) e^{\frac{i2\pi(k-1)z_l}{L}}, \qquad (6b)$$

$$\hat{\omega}_z(\beta_j, k, t) = \sum_{l=0}^{M} \left(\frac{2}{R_o^2 [J_0(\beta_j)]^2} \int_0^{R_o} \omega_z(r, z_l, t) J_0\left(\frac{\beta_j r}{R_o}\right) r\, dr \right) e^{\frac{i2\pi(k-1)z_l}{L}}, \qquad (6c)$$

and $z_l = (l-1)L/M$, $l = 1, \ldots, M$ are the mesh points of the discrete axial Fourier transform. The kernel for Bessel transform is based on the eigenfunctions of the curl operator $(3a$–$c)$.

The transform $\hat{\omega}$ of ω splits into left- and right-handed parts as

$$\hat{\omega}(\beta_j, k, t) = \hat{\omega}_r e_r + \hat{\omega}_\theta e_\theta + \hat{\omega}_z e_z = a_{j,k}(t)\,\hat{R}_{j,k} + b_{j,k}(t)\,\hat{L}_{j,k}, \qquad (7)$$

where

$$\hat{R}_{j,k} = \frac{k^2}{2\lambda_{j,k}^2}\left(e_r + \frac{i\lambda_{j,k}}{k}e_\theta + \frac{iq_j}{k}e_z\right), \quad \hat{R}_{j,0} = \tfrac{1}{2}(e_\theta + e_z),$$

$$\hat{L}_{j,k} = \frac{k^2}{2\lambda_{j,k}^2}\left(e_r - \frac{i\lambda_{j,k}}{k}e_\theta + \frac{iq_j}{k}e_z\right), \quad \hat{L}_{j,0} = \tfrac{1}{2}(-e_\theta + e_z),$$

are the normalized Bessel–Fourier transforms of V^+ and V^-, respectively, and $a_{j,k}$, $b_{j,k}$ are obtained by applying projection operators $\hat{P}^+$, $\hat{P}^-$:

$$a_{j,k}(t) \equiv \hat{P}^+[\hat{\omega}] \equiv \hat{\omega} \cdot \hat{R}_{j,k}^*, \quad b_{j,k}(t) \equiv \hat{P}^-[\hat{\omega}] \equiv \hat{\omega} \cdot \hat{L}_{j,k}^*. \qquad (8a,b)$$

A consequence of this decomposition is that by inverse Bessel–Fourier transform of $a_{j,k}$ or $b_{j,k}$ we obtain the ω_R or ω_L fields separately as follows:

$$\omega_R = \frac{1}{2M} \sum_{k=-M/2+1}^{M/2} \sum_{j=1}^{N} (a_{j,k} V_{j,k}^+ + a_{j,k}^* V_{j,k}^{+*}), \qquad (9a)$$

$$\omega_L = \frac{1}{2M} \sum_{k=-M/2+1}^{M/2} \sum_{j=1}^{N} (b_{j,k} V_{j,k}^- + b_{j,k}^* V_{j,k}^{-*}). \qquad (9b)$$

In Bessel–Fourier space, the velocity field $(\hat{\boldsymbol{u}}(\beta_j, k, t) = \hat{u}_r \boldsymbol{e}_r + \hat{u}_\theta \boldsymbol{e}_\theta + \hat{u}_z \boldsymbol{e}_z)$ corresponding to the vorticity field $\hat{\omega}(\beta_j, k, t)$ is given by

$$\hat{\boldsymbol{u}} = \left(\frac{a_{j,k}}{\lambda_{j,k}} \hat{\boldsymbol{R}}_{j,k} - \frac{b_{j,k}}{\lambda_{j,k}} \hat{\boldsymbol{L}}_{j,k} \right)$$

$$= \frac{k^2}{2\lambda_{j,k}^2} \left[\frac{1}{\lambda_{j,k}} (a_{j,k} - b_{j,k}) \boldsymbol{e}_r + \frac{\mathrm{i}}{k} (a_{j,k} + b_{j,k}) \boldsymbol{e}_\theta + \frac{\mathrm{i} q_j}{k \lambda_{j,k}} (a_{j,k} - b_{j,k}) \boldsymbol{e}_z \right]. \tag{10}$$

Inverse Bessel–Fourier transform is used to transform $\hat{\boldsymbol{u}}$ into physical space as follows:

$$u_r(r, z_l, t) = \frac{1}{M} \sum_{k=-M/2+1}^{M/2} \sum_{j=1}^{N} \left(\hat{u}_r(\beta_j, k, t) J_1 \left(\frac{\beta_j r}{R_0} \right) \right) \mathrm{e}^{\frac{-\mathrm{i}2\pi(k-1)z_l}{L}}, \tag{11a}$$

$$u_\theta(r, z_l, t) = \frac{1}{M} \sum_{k=-M/2+1}^{M/2} \sum_{j=1}^{N} \left(\hat{u}_\theta(\beta_j, k, t) J_1 \left(\frac{\beta_j r}{R_0} \right) \right) \mathrm{e}^{\frac{-\mathrm{i}2\pi(k-1)z_l}{L}}, \tag{11b}$$

$$u_z(r, z_l, t) = \frac{1}{M} \sum_{k=-M/2+1}^{M/2} \sum_{j=1}^{N} \left(\hat{u}_z(\beta_j, k, t) J_0 \left(\frac{\beta_j r}{R_0} \right) \right) \mathrm{e}^{\frac{-\mathrm{i}2\pi(k-1)z_l}{L}}. \tag{11c}$$

Also, since V is divergence-free, both $\boldsymbol{u}$ and ω are divergence-free at all times.

The quantity $\boldsymbol{u} \times \omega$ is calculated at z_l and Gauss–Legendre quadrature points used to evaluate the integrals in the Bessel transform. Then $\boldsymbol{u} \times \omega$ is transformed to Bessel–Fourier space and projected onto eigenfunctions of the curl operator. Two-thirds truncation is used in the axial direction to remove aliasing errors. Note that besides the right- and left-handed rotational components of $\boldsymbol{u} \times \omega$, which can be projected onto the eigenfunctions of the curl operator, a component corresponding to non-zero divergence also exists. The latter determines the pressure distribution necessary to maintain a divergence-free velocity field. A consequence of this non-zero divergence is that while projecting $\boldsymbol{u} \times \omega$ we need to explicitly transform its radial component. This is unlike the case of velocity and vorticity fields, where only azimuthal and axial components need to be transformed, because the solenoidality of these provides a linear relation between the radial and axial components in the transformed space.

Thus, the vorticity transport equation in transformed space becomes

$$\frac{\mathrm{d}a_{j,k}(t)}{\mathrm{d}t} = \lambda_{j,k} \hat{P}^+ \overbrace{[\boldsymbol{u} \times (\omega \times 2\Omega \boldsymbol{e}_z)]} - \lambda_{j,k}^2 \nu a_{j,k}(t), \tag{12a}$$

$$\frac{\mathrm{d}b_{j,k}(t)}{\mathrm{d}t} = -\lambda_{j,k} \hat{P}^- \overbrace{[\boldsymbol{u} \times (\omega \times 2\Omega \boldsymbol{e}_z)]} - \lambda_{j,k}^2 \nu b_{j,k}(t). \tag{12b}$$

These ordinary differential equations are solved using a fifth-order six-stage Runge–Kutta scheme (Lambert 1983, p. 143). Computationally, the most expensive part of this algorithm is Bessel transform evaluations. Of these, Bessel function calculation costs the most, so these were evaluated during initialization and stored for later time advancement. Using Cray scientific library routines, very efficient Bessel transforms (294MFlops on Cray-YMP) were implemented. Overall performance of the code was 172MFlops. The ratio of operation count for our algorithm to that for a hypothetical FFT algorithm for both the r- and z-directions is 11.5 for the resolution
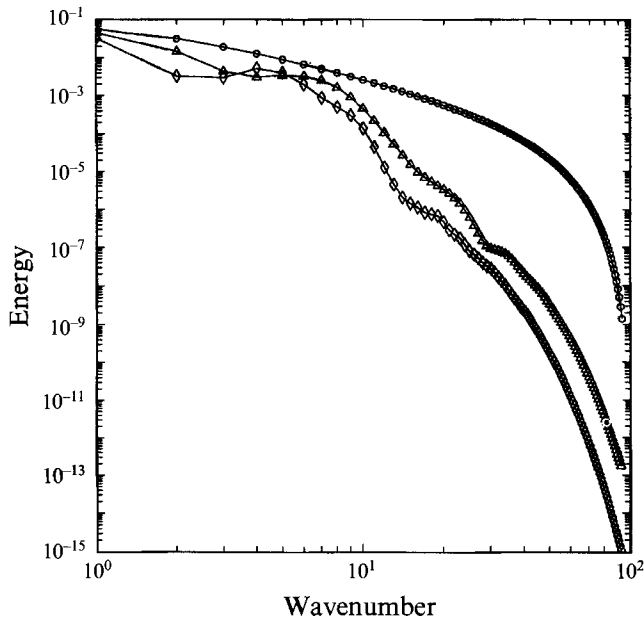
FIGURE 2. Energy spectra for case E ($\chi = 0$, $Re = 800$) at $T = 0$ ($\bigcirc$), $T = 80$ ($\triangle$), $T = 150$ ($\diamondsuit$).

used in the present simulations. This increase in operation count is due to the lack of a fast (Bessel) transform in r.

The boundary conditions shown in figure 1(d) imply that if velocity is expanded in $V^-_{j,k}$ and $V^+_{j,k}$ the circulation ($\Gamma_z = R_o u_\theta(r = R_o)$) is zero. This is clearly satisfied for unpolarized rings. For polarized rings, the radial extent of the domain is chosen large enough that u_θ near the outer boundary is of the order of machine accuracy.

2.3. *Validation of the code*

We reproduced results computed by Stanaway, Cantwell & Spalart (1988). Our results on the evolution of Re, U_p (see (31)), and rate of change of energy and dissipation agree with those of Stanaway *et al.* Moreover, the linear impulse deviated from its initial value by less than 10^{-9} in our case, while Stanaway *et al.* reported a deviation of 10^{-4}. The reason for their larger error is that their grid is non-uniform and, as the vortex diffused, the vorticity gradient became significant in lower-resolution regions. In our uniform grid, resolution improves as the ring diffuses. Another test case used for code validation was the evolution of a columnar vortex with non-uniform cross-section simulated by Melander & Hussain (1993) using a three-dimensional spectral code with periodic boundary conditions. Again, good agreement was obtained. Energy spectra along the axial direction shown in figure 2 (after integration in radial direction) for the high-Re case E (discussed below) show that the simulations are well resolved.

2.4. *Initial conditions*

Initial conditions are constructed from unpolarized rings with a circular cross-section and azimuthal vorticity profile

$$\omega_\theta = \begin{cases} \omega_o \exp(-4\zeta^2/(1-\zeta^2)) \exp(4\zeta^4 + 4\zeta^6 + 4\zeta^8), & 0 \leqslant \zeta < 1 \\ 0 & 1 \leqslant \zeta, \end{cases} \tag{13}$$
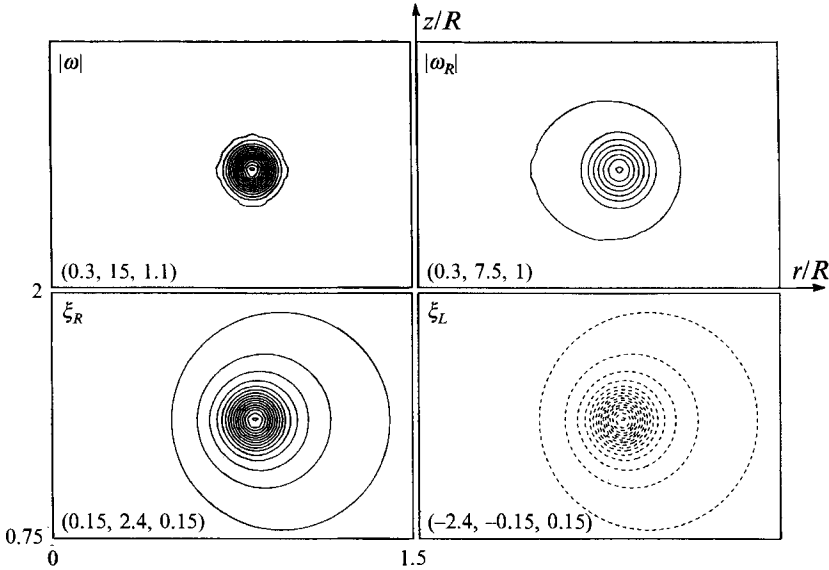
FIGURE 3. Polarized components of a vortex ring. $|\omega_\theta|$ in the polarized components is half of that in an unpolarized ring and the contours (not shown) are the same as those for $|\omega|$ with half the magnitude. The axial and radial vorticity components are shown by ξ (defined in (16)). The contour levels (min., max., increment) are indicated in the figure.

where $\zeta = [(r-r_c)^2 + (z-z_c)^2]^{\frac{1}{2}}/a$. This is nearly Gaussian for $\zeta \ll 1$ and has a compact support; i.e. ω_θ is zero outside the core radius a.

This unpolarized ring is specified in physical space. We then transform it to Bessel–Fourier space and decompose it into left- and right-handed components, ω_R and ω_L. A new vortex ring with initial vorticity (ω_{IC}) is then constructed as

$$\omega_{IC} = \omega_R + \chi\omega_L, \tag{14}$$

where $(1-\chi)$ is the *degree of polarization*. That is, $\chi = 0$ represents a *fully* polarized right-handed ring, while $\chi = 1$ denotes *no* polarization. The left- and right-handed components of (13) are shown in figure 3. ω_θ has the same sign but half the magnitude of the original vortex for the two components. Therefore, both components have a curvature-induced velocity in the same direction. The opposite polarity arises from opposite-signed distributions of ω_r and ω_z. This is most clearly seen by considering a cross-section of axisymmetric vortex surfaces for the right- and left-handed components. To obtain these surfaces, a function $\xi(r,z)$ may be introduced such that

$$\frac{\partial \xi}{\partial z} = -r\omega_r, \quad \frac{\partial \xi}{\partial r} = r\omega_z. \tag{15}$$

In a meridional (i.e. (r,z)) plane, $(\omega_r \boldsymbol{e}_r + \omega_z \boldsymbol{e}_z)$ is tangent to contours of constant ξ. Hence, $\xi(r,z)$ contours are axisymmetric vortex surfaces, which can be found from the relation $\nabla \times u_\theta \boldsymbol{e}_\theta = \omega_r \boldsymbol{e}_r + \omega_z \boldsymbol{e}_z = \nabla \times (\xi/r) \boldsymbol{e}_\theta$, i.e.

$$\xi = ru_\theta. \tag{16}$$

Figure 3 shows that the left- and right-handed components of ξ have opposite signs. The vortex lines wind as left- and right-handed helices for the left- and right-handed

Case	Re	χ
A	800	1.0
B	150	1.0
C	800	0.75
D	800	0.5
E	800	0.00
F	150	0.75
G	150	0.50
H	150	0.25
I	150	0.125
J	150	0.00
K	800	-1.00

TABLE 1. List of simulations. In these computations, a/R, the ratio of core to ring radii, was 0.2. The radial and axial extents of the computational domains were 10 and 15 ring radii, respectively. The Bessel transform was evaluated by first dividing the radial extent into 20 subintervals and then using a Gauss–Legendre quadrature rule of order 20 in each subinterval. 384 collocation points were used in the axial direction, and first 200 zeros of J_1 were considered for the Bessel transform.

components, respectively. The induced u_θ is into the page for ω_R and out of the page for ω_L. Note that the polarized ξ-components are non-zero even in the region where ω_θ vanishes; i.e. u_θ is non-zero even outside the region where ω_θ is zero. In this study, $0 \leqslant \chi \leqslant 1$. However, right-handed-dominated rings can also have χ between -1 and 0. Such rings would have higher swirl than considered here. Actually, $\chi = -1$ would be a torus with only u_θ and zero ω_θ.

The linear impulse ($I = \pi \int \omega_\theta r^2 \, dr \, dz$) of all rings in the present study is the same. Therefore, we may think of rings with different χ as being generated by a piston with the same axial force but different torque acting on it. The Reynolds number (Γ/ν) is an independent parameter for such vortices. Initial conditions for all simulations are given in table 1.

2.5. Non-dimensional timescales

In order to non-dimensionalize time, it is assumed that a line vortex ring formed at $t = 0$ decays self-similarly with peak vorticity decaying as $(1/t)$ and lengthscale increasing as $(\nu t)^{\frac{1}{2}}$, where t is time and ν is kinematic viscosity (Stanaway *et al.* 1988). Thus, finite-core rings used in initial conditions for simulations are assumed to be the result of self-similar decay of a line vortex. The time origin is defined by comparison with the Oseen solution, i.e. $t_o = \Gamma/4\pi\nu\omega_o$, where Γ is circulation, and ω_o is defined in (13) above. Thus, time is non-dimensionalized as

$$t_\Gamma = (t + t_o)\,\nu/R^2. \tag{17}$$

In the following, T denotes dimensional time with origin at the beginning of the simulation. The relation for non-dimensional time is $t_\Gamma = (T+0.79577)\,2.7833 \times 10^{-3}$ for $Re = 150$ and $t_\Gamma = (T+4.24413)\,5.2187 \times 10^{-4}$ for $Re = 800$. At $T = 0$, the maximum value of η is 7.5 m^{-1} s^{-1} and of ξ (for fully polarized case) is 4.85 m^2 s^{-1}. The dimensions of η and ξ remain the same throughout the paper and are not repeated.

3. Coupling between meridional flow and swirl

The evolution equations for the meridional flow $\eta \equiv \omega_\theta / r$ and swirl $\xi \equiv r u_\theta$ are

$$\frac{\mathrm{D}\eta}{\mathrm{D}t} \equiv \frac{\partial \eta}{\partial t} + u_r \frac{\partial \eta}{\partial r} + u_z \frac{\partial \eta}{\partial z} = \frac{1}{r^4} \frac{\partial \xi^2}{\partial z} + \nu \left[\frac{\partial^2 \eta}{\partial r^2} + \frac{3}{r} \frac{\partial \eta}{\partial r} + \frac{\partial^2 \eta}{\partial z^2} \right], \qquad (18\,a)$$

$$\frac{\mathrm{D}\xi}{\mathrm{D}t} = \nu \left[\frac{\partial^2 \xi}{\partial r^2} - \frac{1}{r} \frac{\partial \xi}{\partial r} + \frac{\partial^2 \xi}{\partial z^2} \right], \qquad (18\,b)$$

$$\eta = \frac{1}{r^2} \frac{\partial^2 \psi}{\partial r^2} - \frac{1}{r^3} \frac{\partial \psi}{\partial r} + \frac{1}{r^2} \frac{\partial^2 \psi}{\partial z^2}, \qquad (18\,c)$$

where $\mathrm{D}/\mathrm{D}t$ is the material derivative following a particle in the meridional flow, and ψ is the meridional stream function.

From (18 a) it is clear that η of a fluid particle is conserved in an inviscid swirl-free flow. The first term on the right-hand side of (18 a) arises from the coupling between meridional flow and swirl. To physically interpret this term, consider the angular velocity ($\dot{\theta} \equiv u_\theta / r$) along a vortex line. If s is the arclength along the vortex line (s increases in the direction of vorticity), then

$$\frac{\partial \dot{\theta}}{\partial s} = \frac{1}{|\omega|} \left(\omega_r \frac{\partial}{\partial r} + \omega_z \frac{\partial}{\partial z} + \omega_\theta \frac{\partial}{r\,\partial \theta} \right) \dot{\theta}.$$

For an axisymmetric flow, the last term on the right-hand side vanishes. Since the vortex line lies on a vortex surface defined by $\xi = \xi_o$, (15), the above equation becomes

$$\frac{\partial \dot{\theta}}{\partial s} = \frac{\xi}{|\omega|} \left(\omega_r \frac{\partial}{\partial r} \right) \frac{1}{r^2} = -\frac{2}{|\omega|} \frac{r \omega_r \xi}{r^4} = \frac{2\xi}{|\omega| r^4} \frac{\partial \xi}{\partial z}.$$

The coupling term is thus

$$\frac{1}{r^4} \frac{\partial \xi^2}{\partial z} = |\omega| \frac{\partial \dot{\theta}}{\partial s}. \qquad (19)$$

This equation highlights the physics behind the coupling term. Namely, it expresses the twisting of vortex lines confined to the surface $\xi = \xi_o$. A vortex line on this surface has $\dot{\theta} = \xi_o / r^2$. Consequently, $|\dot{\theta}|$ increases where the vortex line curves inwards ($\partial r / \partial s < 0$) and decreases where it bends outwards ($\partial r / \partial s > 0$). Hence there is an exchange between meridional and azimuthal vorticity where the $\xi = \xi_o$ surface is not parallel to the z-axis. This has a profound effect on the evolution of η, for η is subject to both material transport as well as generation and destruction by twisting of vortex lines. Our vortex rings propagate either up or down along the z-axis. Which direction a given ring moves in depends on $s_\eta \equiv \mathrm{sgn}(\int \eta \, \mathrm{d}r \, \mathrm{d}z)$. s_η is positive for ascending and negative for descending rings, and does not change during the evolutions. The propagation direction defines the ring's *front* and *rear*. From (19) we then at once find that η^2 is destroyed in the front and generated in the rear by the coupling term (figure 4). This effect increases with the magnitude of ξ and hence with the degree of polarization $(1 - \chi)$.
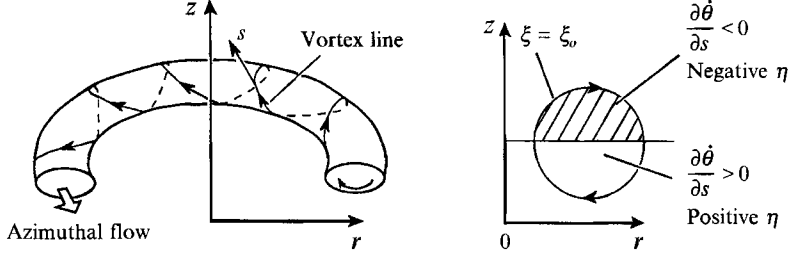
FIGURE 4. Schematic to show the generation of η via the coupling term for a right-handed ring. The projection of a vortex line in a meridional plane is shown on the right. Irrespective of the polarity of the ring, negative η is generated in front and positive η is generated at the back of the vortex ring.

4. Equations for the interaction of polarized components

As discussed above, axisymmetric flows are best analysed in terms of ξ, η, and ψ. We therefore also consider the polarized components of these variables. This requires slightly different projection operators, because the projection operators defined in §2.2 are for a three-component vector and cannot be used directly here. The new projection method is based on the expansions

$$\boldsymbol{u} = \sum [c_{j,k}\, \boldsymbol{V}_{j,k}^{+} + d_{j,k}\, \boldsymbol{V}_{j,k}^{-}], \quad \boldsymbol{\omega} = \sum [\lambda_{j,k} c_{j,k}\, \boldsymbol{V}_{j,k}^{+} - \lambda_{j,k} d_{j,k}\, \boldsymbol{V}_{j,k}^{-}]. \quad (20a, b)$$

Using (4) we obtain the following expansions of the azimuthal components:

$$u_\theta = \sum A_u\, J_1(q_j r)\, e^{ikz} = \sum [c_{j,k} - d_{j,k}] \frac{i\lambda_{j,k}}{k} J_1(q_j r)\, e^{ikz}, \quad (21a)$$

$$\omega_\theta = \sum A_\omega\, J_1(q_j r)\, e^{ikz} = \sum [c_{j,k} + d_{j,k}] \frac{i\lambda_{j,k}^2}{k} J_1(q_j r)\, e^{ikz}. \quad (21b)$$

From the orthogonality properties of J_1 and of exponential function, it follows that

$$A_u = \hat{u}_\theta, \quad A_\omega = \hat{\omega}_\theta. \quad (22)$$

Therefore, $\qquad \hat{u}_\theta = \dfrac{i\lambda_{j,k}}{k}(c_{j,k} - d_{j,k}), \quad \hat{\omega}_\theta = \dfrac{i\lambda_{j,k}^2}{k}(c_{j,k} + d_{j,k})$

or, $\qquad c_{j,k} = \dfrac{-ik}{2\lambda_{j,k}}\left(\hat{u}_\theta + \dfrac{\hat{\omega}_\theta}{\lambda_{j,k}}\right) \quad$ and $\quad d_{j,k} = \dfrac{-ik}{2\lambda_{j,k}}\left(-\hat{u}_\theta + \dfrac{\hat{\omega}_\theta}{\lambda_{j,k}}\right).$ $\qquad (23)$

The right- and left-handed components of ξ and η can then be expressed as

$$\xi_R = r \sum c_{j,k}\left(\frac{i\lambda_{j,k}}{k}\right) J_1(q_j r)\, e^{ikz}, \quad \xi_L = -r \sum d_{j,k}\left(\frac{i\lambda_{j,k}}{k}\right) J_1(q_j r)\, e^{ikz}, \quad (24a)$$

$$\eta_R = \frac{1}{r} \sum c_{j,k}\left(\frac{i\lambda_{j,k}^2}{k}\right) J_1(q_j r)\, e^{ikz}, \quad \eta_L = \frac{1}{r} \sum d_{j,k}\left(\frac{i\lambda_{j,k}^2}{k}\right) J_1(q_j r)\, e^{ikz}. \quad (24b)$$

Now, using the same procedure we can obtain projections of any two terms from the equations for ξ and η. For the right-handed components, these equations become

$$
\frac{\partial}{\partial t}\begin{pmatrix} \eta_R \\ \xi_R \end{pmatrix} = -\underbrace{\begin{pmatrix} u_{rR}\dfrac{\partial \eta_R}{\partial r}+u_{zR}\dfrac{\partial \eta_R}{\partial z}-\dfrac{1}{r^4}\dfrac{\partial \xi_R^2}{\partial z} \\[2ex] u_{rR}\dfrac{\partial \xi_R}{\partial r}+u_{zR}\dfrac{\partial \xi_R}{\partial z} \end{pmatrix}}_{\text{I}} - \underbrace{\begin{pmatrix} u_{rL}\dfrac{\partial \eta_R}{\partial r}+u_{zL}\dfrac{\partial \eta_R}{\partial z} \\[2ex] u_{rL}\dfrac{\partial \xi_R}{\partial r}+u_{zL}\dfrac{\partial \xi_R}{\partial z} \end{pmatrix}}_{\text{II}}
$$

$$
+P^-\underbrace{\begin{pmatrix} u_r\dfrac{\partial \eta_R}{\partial r}+u_z\dfrac{\partial \eta_R}{\partial z}-\dfrac{1}{r^4}\dfrac{\partial \xi_R^2}{\partial z} \\[2ex] u_r\dfrac{\partial \xi_R}{\partial r}+u_z\dfrac{\partial \xi_R}{\partial z} \end{pmatrix}}_{\text{III}} - P^+\underbrace{\begin{pmatrix} u_r\dfrac{\partial \eta_L}{\partial r}+u_z\dfrac{\partial \eta_L}{\partial z}-\dfrac{1}{r^4}\dfrac{\partial \xi_L^2}{\partial z} \\[2ex] u_r\dfrac{\partial \xi_L}{\partial r}+u_z\dfrac{\partial \xi_L}{\partial z} \end{pmatrix}}_{\text{IV}}
$$

$$
+2P^+\underbrace{\begin{pmatrix} \dfrac{1}{r^4}\dfrac{\partial(\xi_R\xi_L)}{\partial z} \\[2ex] 0 \end{pmatrix}}_{\text{V}} + \nu P^+\underbrace{\begin{pmatrix} \dfrac{\partial^2 \eta_R}{\partial r^2}+\dfrac{\partial^2 \eta_R}{\partial z^2}+\dfrac{3}{r}\dfrac{\partial \eta_R}{\partial r} \\[2ex] \dfrac{\partial^2 \xi_R}{\partial r^2}+\dfrac{\partial^2 \xi_R}{\partial z}-\dfrac{1}{r}\dfrac{\partial \xi_R}{\partial r} \end{pmatrix}}_{\text{VI}}. \tag{25}
$$

Here P^+ and P^- are the operations defined in (22)−(24); $\hat{u}_\theta$ is replaced by $\hat{C}_\xi$ and $\hat{\omega}_\theta$ by $\hat{C}_\eta$, where $\hat{C}_\eta$ and $\hat{C}_\xi$ are the Bessel–Fourier space representations of the top and bottom terms in (25) (before taking Bessel–Fourier transforms, the top term is multiplied by r and the bottom term is divided by r). Written in the above form, (25) allows separation of terms due to interaction of polarized components from those in the ξ- and η-equations. Physically the terms in (25) are: (I) the self-evolution of η_R and ξ_R, (II) advection of η_R and ξ_R by left-handed velocity, (III) generation of η_L and ξ_L due to evolution of η_R and ξ_R, (IV) generation of η_R and ξ_R due to evolution of η_L and ξ_L, (V) coupling between the left- and right-handed swirl and meridional flow, and (VI) viscous decay. Evolution equations for ξ_L and η_L can be obtained from (25) by interchanging R and L as well as P^+ and P^-.

5. Numerical simulations – observations

5.1. *Persistence of polarization*

The kinetic energy (E), enstrophy (Z) and helicity (H) can be decomposed into right- and left-handed contributions:

$$
E = E_R+E_L, \quad E_R = \int u_R\cdot u_R\,dV, \quad E_L = \int u_L\cdot u_L\,dV, \tag{26a}
$$

$$
Z = Z_R+Z_L, \quad Z_R = \int \omega_R\cdot \omega_R\,dV, \quad Z_L = \int \omega_L\cdot \omega_L\,dV, \tag{26b}
$$

$$
H = H_R+H_L, \quad H_R = \int u_R\cdot \omega_R\,dV, \quad H_L = \int u_L\cdot \omega_L\,dV. \tag{26c}
$$

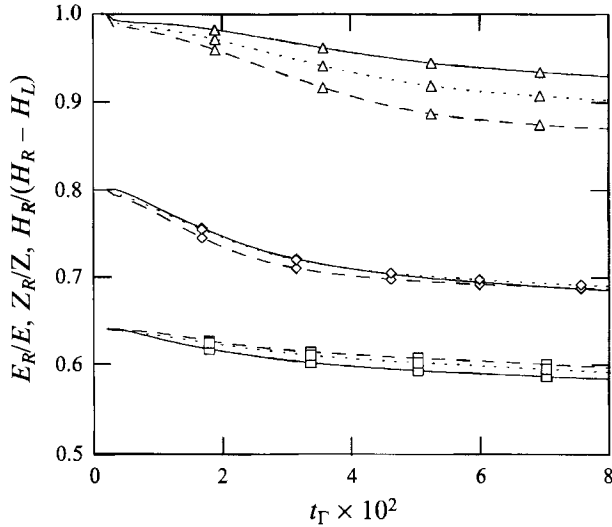Here integration is over the entire three-dimensional domain. Integrals of the cross-

FIGURE 5. Evolution of kinetic energy $E_R/(E_R+E_L)$ (solid line), enstrophy $Z_R/(Z_R+Z_L)$ (dashed line), and helicity $H_R/(H_R-H_L)$ (dotted line) for $Re = 800$ cases E ($\triangle$, $\chi = 0$), D ($\diamond$, $\chi = 0.5$) and C ($\square$, $\chi = 0.75$).

terms like $(u_R \cdot u_L)$ vanish due to orthogonality of the right- and left-handed fields. For unpolarized flows, $E_R/E = Z_R/Z = H_R/(H_R-H_L) = 0.5$. During the evolution of our initially polarized rings, these ratios remain nearly constant; only 12% variation is observed in $Re = 800$ cases (C, D and E) shown in figure 5, and 5% in $Re = 150$ cases F–J (not shown). The evolutions of these quantities are uneventful slow decays as shown in figure 5. Thus, isolated polarized vortical structures retain most of their polarization.

The degree of polarization $(1-\chi)$ is initially constant, but becomes spatially non-uniform during the evolution. The spatial variations can be represented by $R_a(r,z) = \log_2(|\omega_R|/|\omega_L|)$, which is zero where both the polarized components are equal in magnitude, *positive* where the right-handed component dominates (i.e. right-polarized) and *negative* where the vorticity is left-polarized. R_a is shown in figure 6 at late times in the evolution of cases D and E. We note that left-handed-dominated regions form, even in case E where the initial ring was completely right-handed (figure 6*b*). However, the ring core remains right-handed. Near the axis strong right-handedness can be see in the wake of the vortex. In the low-*Re* cases, the results are similar, except that a left-handed-dominated region (i.e. $R_a < 0$) is not seen for the fully polarized case.

5.2. *Unpolarized reference cases*

Figure 7(*a, b*) shows the evolution of ω_θ (or $|\omega|$) in unpolarized rings. In case A (*Re* = 800), the ring shows the typical head–tail structure observed by Shariff *et al.* (1988). In case B (*Re* = 150), the tail is much thicker and not clearly separated from the head. Maxworthy (1972) has proposed a mechanism for tail formation involving diffusion of vorticity across the vortex bubble and its subsequent detrainment near the rear stagnation point. The thicker tail formed at lower *Re* is consistent with this explanation. However, tail formation in inviscid simulations (Shariff *et al.*) suggests that there is an additional inviscid mechanism.

In analysing axisymmetric flows without swirl, $\eta \equiv \omega_\theta/r$ and the meridional stream function ψ in a frame moving with U_p, (31), are very informative. This is because η is
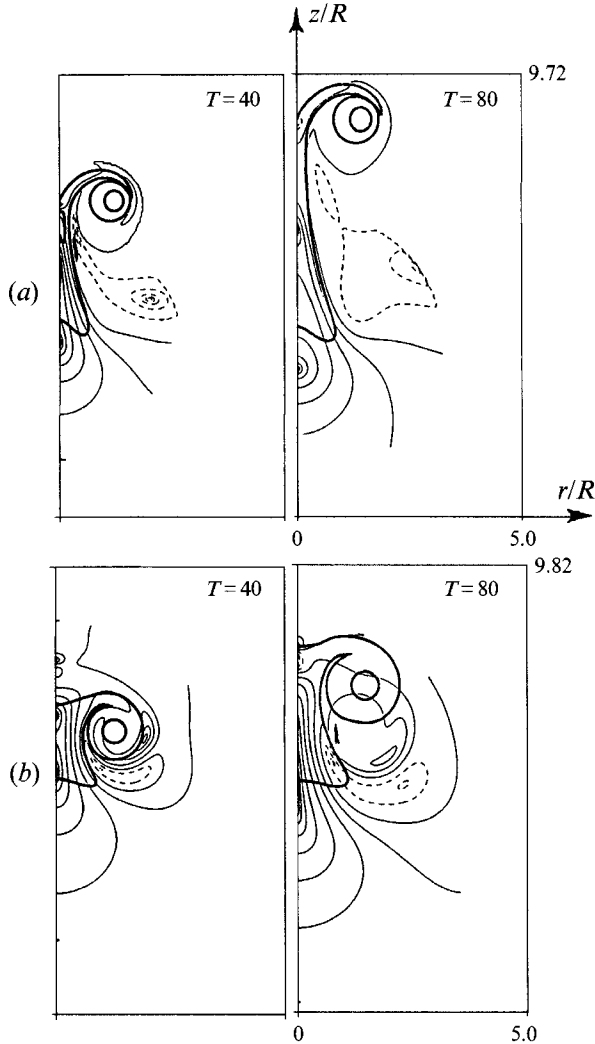
FIGURE 6. Spatial distribution of polarization ($R_a = \log_2(|\omega_R|/|\omega_L|)$) for $Re = 800$ cases. Only a part of the domain is shown. Regions where $|\omega| < 10^{-3}\omega_{peak}$ are excluded. (a) Case D ($\chi = 0.5$); contour levels (min., max.) with increment $= 1$ are: $T = 40$ (-5, 10.58), $T = 80$ (-4.65, 9.4). (b) Case E ($\chi = 0$); contour levels with increment $= 1$ are: $T = 40$ (-1.51, 11.8), $T = 80$ (-5.51, 9.55). Thick lines are overlayed contours of $|\omega|$: $T = 40$ (0.15, 0.85), $T = 80$ (0.08, 0.48). In this plot we use periodicity in z-direction to get tail region behind the head.

advected with the meridional velocity in an inviscid, swirl-free flow, (18a). If, moreover, the flow is steady in some reference frame, then $\eta = \eta(\psi)$. In figure 8, contours of η and ψ are overlaid. In the high-Re case (A) these contours are nearly aligned in the core and resemble boundaries of steady inviscid Norbury vortices (Norbury 1973). Hence Re is sufficiently large for the deformation of the ring core to be negligible on a convective timescale (turnover time T_t, defined as that required for a particle at the core radius a to go around the core once, is $O(6\pi/\omega_o)$; a and ω_o are defined in (13)). The contours in figure 8(a) appear after approximately $110T_t$. This alignment of ω_θ and ψ was also observed by Stanaway *et al.* (1988). In the low-Re case B, the ψ- and η-contours soon become misaligned, and the core cross-section is,

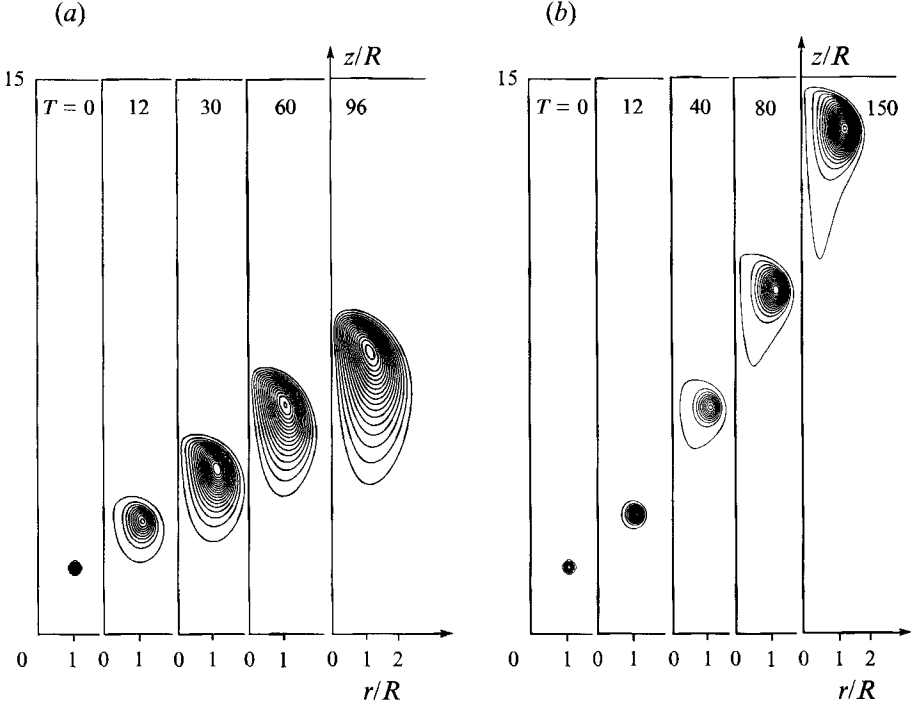FIGURE 7. (a) ω_θ contours for unpolarized $Re = 150$ case B. Only a part of the domain is shown. The peak values are: $T = 0$ (15), $T = 12$ (0.95), $T = 30$ (0.374), $T = 60$ (0.171), $T = 96$ (0.092). (b) ω_θ contours for unpolarized case A ($Re = 800$). Only a part of the domain is shown. The peak values are: $T = 0$ (15), $T = 12$ (4.09), $T = 40$ (1.42), $T = 80$ (0.755), $T = 150$ (0.416). In each frame, the contour levels are equispaced.

consequently, very different from the inviscid steady solutions of Norbury; see figure 8(b) (shown after approximately $70T_t$). Thus, diffusion of vorticity at very low Re can lead to a misalignment of ψ- and η-contours, i.e. core deformation by advection.

The η-contours show the location of viscous vorticity annihilation. To demonstrate this, note that the z-axis is a material line that can be closed at infinity into a material circuit C encompassing the entire meridional plane. Thereby (Batchelor 1967, p. 269)

$$\frac{\mathrm{d}\Gamma}{\mathrm{d}t} = -\nu \int_C (\nabla \times \omega) \cdot \mathrm{d}l \tag{27}$$

$$= -\nu \int_{-\infty}^{+\infty} \frac{1}{r} \frac{\partial}{\partial r} (r\omega_\theta) \Big|_{r=0} \mathrm{d}z = -2\nu \int_{-\infty}^{+\infty} \frac{\omega_\theta}{r} \Big|_{r=0} \mathrm{d}z = -2\nu \int_{-\infty}^{+\infty} \eta \Big|_{r=0} \mathrm{d}z; \tag{28}$$

here we have used L'Hospital rule (i.e. $\omega_\theta(0, z) = 0$, $\lim_{r \to 0}(\omega_\theta/r) = \lim_{r \to 0}(\partial\omega_\theta/\partial r)$). Figure 8 shows that the most intense annihilation of Γ occurs near the front stagnation point, with the least in the tail. Note that (28) is valid irrespective of whether the vortex has swirl or not.

5.3. *Structure of polarized rings*

Figure 9(a) shows the evolution of $|\omega|$ contours for case E ($\chi = 0$, $Re = 800$). Upon comparison with case A ($\chi = 1.0$, $Re = 800$, figure 7b), many differences are readily discerned. The axial motion is drastically reduced in case E and the head–tail structure is very different from that in case A. There is an axial vortex near the axis and an
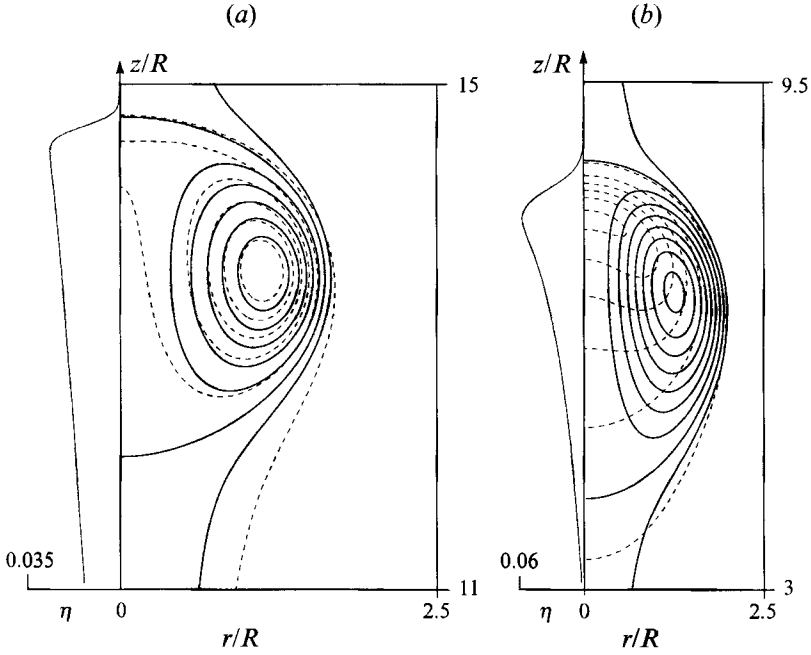
FIGURE 8. η (dashed lines) overlaid on streamlines (solid lines) in a frame moving with the centroid velocity defined in (31) for ($\chi = 1$) cases A and B. Only a part of the domain is shown. (*a*) $Re = 800$, $T = 150$. (*b*) $Re = 150$, $T = 96$. Note the misalignment of contours in the low-Re case. Distribution of η on the axis clearly suggests that most of the circulation annihilation occurs near the front of the ring.
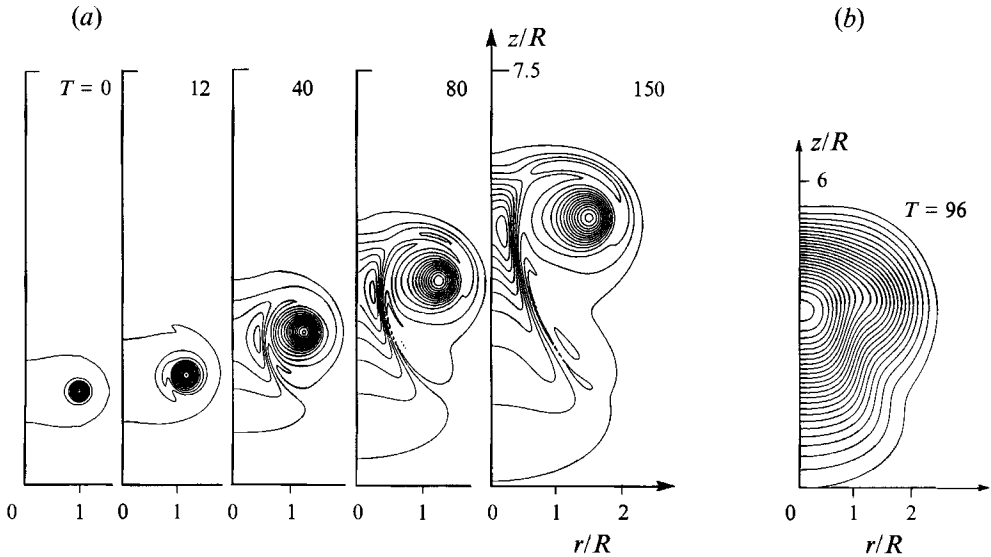

FIGURE 9. (*a*) $|\omega|$ contours for case E ($\chi = 0$, $Re = 800$); only a part of the domain is shown. The peak values are: $T = 0$ (15), $T = 12$ (4.32), $T = 40$ (1.57), $T = 80$ (0.84), $T = 150$ (0.44). (*b*) $|\omega|$ for case J ($\chi = 0$, $Re = 150$) at $T = 96$; the peak values is 0.132; only a part of the domain is shown.
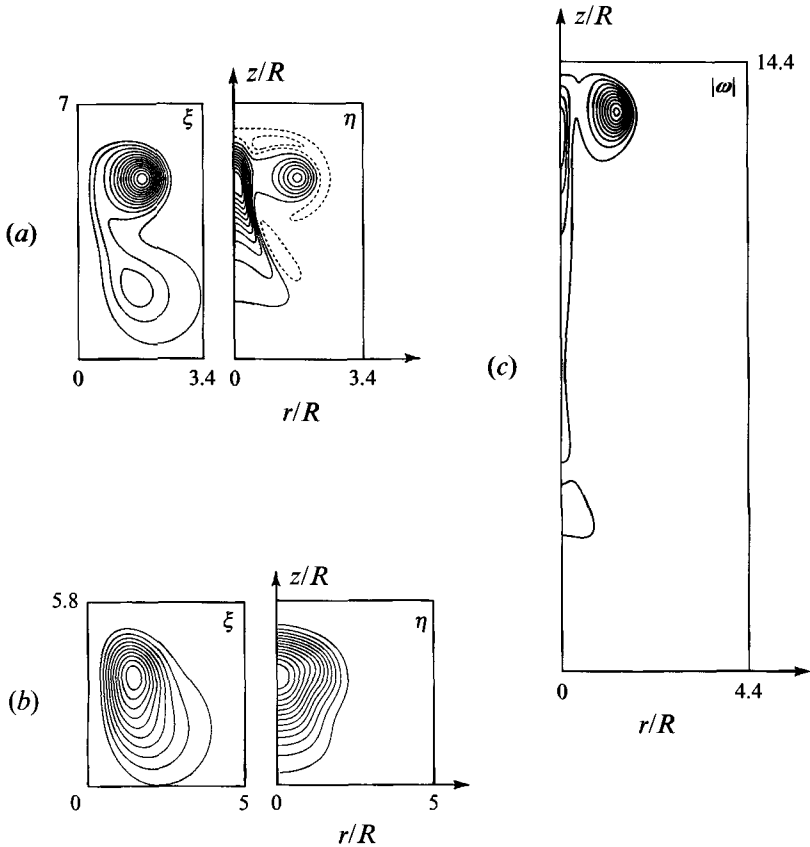
FIGURE 10. (a) ξ and η for case E ($\chi = 0$, $Re = 800$) at $T = 150$. Contour levels (min., max., increment) are: ξ (0.0355, 0.497, 0.0355), η (-0.048, 0.244, 0.021); (b) the same for case J ($\chi = 0$, $Re = 150$) at $T = 96$; ξ (0.038, 0.233, 0.02), η (-0.0009, 0.057, 0.004). (c) $|\omega|$ for case C ($\chi = 0.75$, $Re = 800$) at $T = 150$. Only a part of the domain is shown.

outward movement of the 'head'. At late times, in case J ($\chi = 0$, $Re = 150$, figure 9b), the head and tail are fused together, and it is difficult to infer a ring from the $|\omega|$-contours. In both cases E and J, the ring structure seems enigmatic in terms of $|\omega|$.

To analyse the ring structure, we examine ξ and η. The contours of these quantities are shown in figure 10(a, b) and correspond to the last frame of figure 9(a) and figure 9(b). At high Re, it is clear that the head is part of the original ring. The axial vortex seen in the $|\omega|$ plots is in the region where the ξ-contours are close and nearly parallel to the axis (at the axis $\omega_r = \omega_\theta = 0$). Here, η is large, implying a strong azimuthal turning of vortex lines. Thus, the vortex line geometry is quite complex in this flow (figure 11a). A vortex line trace (figure 11b) on a low ξ-contour (a cross-section of an axisymmetric vortex surface) near the head moves out of the plane first radially outward, then axially downward, then radially inward, and finally changes the azimuthal direction into the plane and moves axially upward. The strong axial vortex is located where the vortex lines spiral upward along the axis. This axial vortex also appears at higher χ; e.g. in figure 10(c) an axial vortex, *apparently* not joined to the ring, is clearly visible. At low Re, ξ and η are more diffused; see figure 10(b). Note that ξ-contours clearly show a ring, again not obvious from $|\omega|$ plot in figure 9(b). As in case B there is no clear head–tail structure.
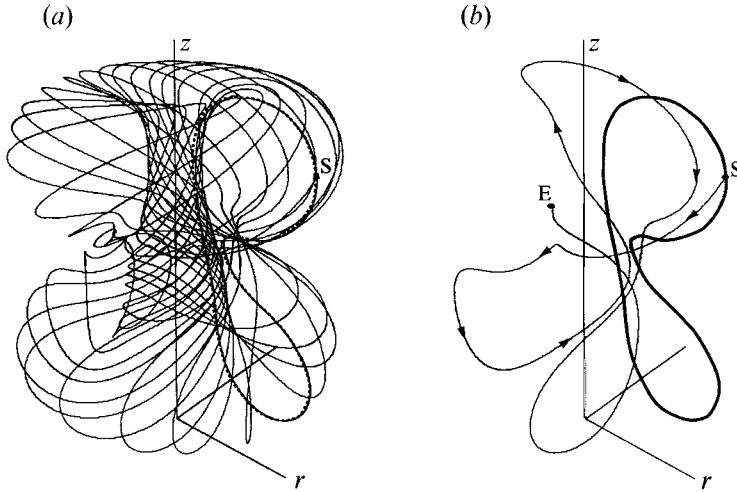
(a)   (b)

FIGURE 11. Vortex line for fully polarized case E ($\chi = 0$, $Re = 800$) at $T = 150$. (a) A vortex line starting at S with trace continued for 5 rotations around the symmetry axis. Note the axial vortex and twisting of vortex lines near the axis. The vortex line does not close for the trace shown and is perhaps surface filling. The cross-section of the vortex surface to which this line is confined is shown by thick dashed line. (b) The same vortex line as in (a) starting at S is traced up to point E. The thick line shows the cross-section of the vortex surface. Arrows are shown only in the first half of the trace for clarity.

5.4. *Topological changes via head–tail formation*

When $\omega_r \equiv \omega_z \equiv 0$ and $\omega_\theta \neq 0$, any closed curve in a meridional plane is the cross-section of a toroidal vortex surface. For a polarized ring, however, only certain curves (namely the ξ-contours) represent toroidal vortex surfaces (16). All polarized simulations initially have the same axisymmetric vortex surfaces (figure 3), only the magnitude of ξ differs. The temporal evolution of ξ is shown in figure 12(a) for case E. The initial peak in ξ corresponds to a closed circular vortex line C_o. Since initially there is only one peak in ξ, all other vortex lines spiral around C_o. Breakup of closed contours by the formation of a new ξ-peak implies that some vortex lines will no longer spiral around C_o and the original vortex core. This requires that vortex lines must have been cut and reconnected at a saddle point in ξ-contours. Owing to axisymmetry, this saddle point also represents a circular vortex line. This reconnection is seen even in low-Re cases and is particularly clear for high χ (figure 13 a, b), because the two ξ-peaks separate quicker due to the faster axial motion. Note that these topological changes cannot be inferred from the $|\omega|$-contours (e.g. figure 10c). In fact, the reconnection occurs at an entirely different place than one might guess based on figure 10(c).

These topological changes represent a new type of vortex reconnection because here the reconnecting vortex lines are locally parallel rather than antiparallel as in previous

FIGURE 12. Evolution of polarized components for case E ($\chi = 0$, $Re = 800$). Only a part of the domain is shown; the minimum and maximum values are: (a) $T = 10$, ξ_L (-0.286, 0.067), ξ_R (0.196, 2.742), ξ (0.175, 2.456); $T = 40$, ξ_L (-0.272, 0.0627), ξ_R (0.106, 1.478), ξ (0.08, 1.21); $T = 80$, ξ_L (-0.276, 0.07), ξ_R (-0.0067, 1.06), ξ (0.063, 0.7846). (b) $T = 10$, η_L (-0.069, 0.212), η_R (-0.065, 1.936), η (-0.086, 2.146); $T = 40$, η_L (-0.12, 0.104), η_R (-0.029, 0.503), η (-0.049, 0.605); $T = 80$, η_L (-0.139, 0.066), η_R (-0.038, 0.296); η (-0.069, 0.294). In each frame, the contour levels are equispaced.
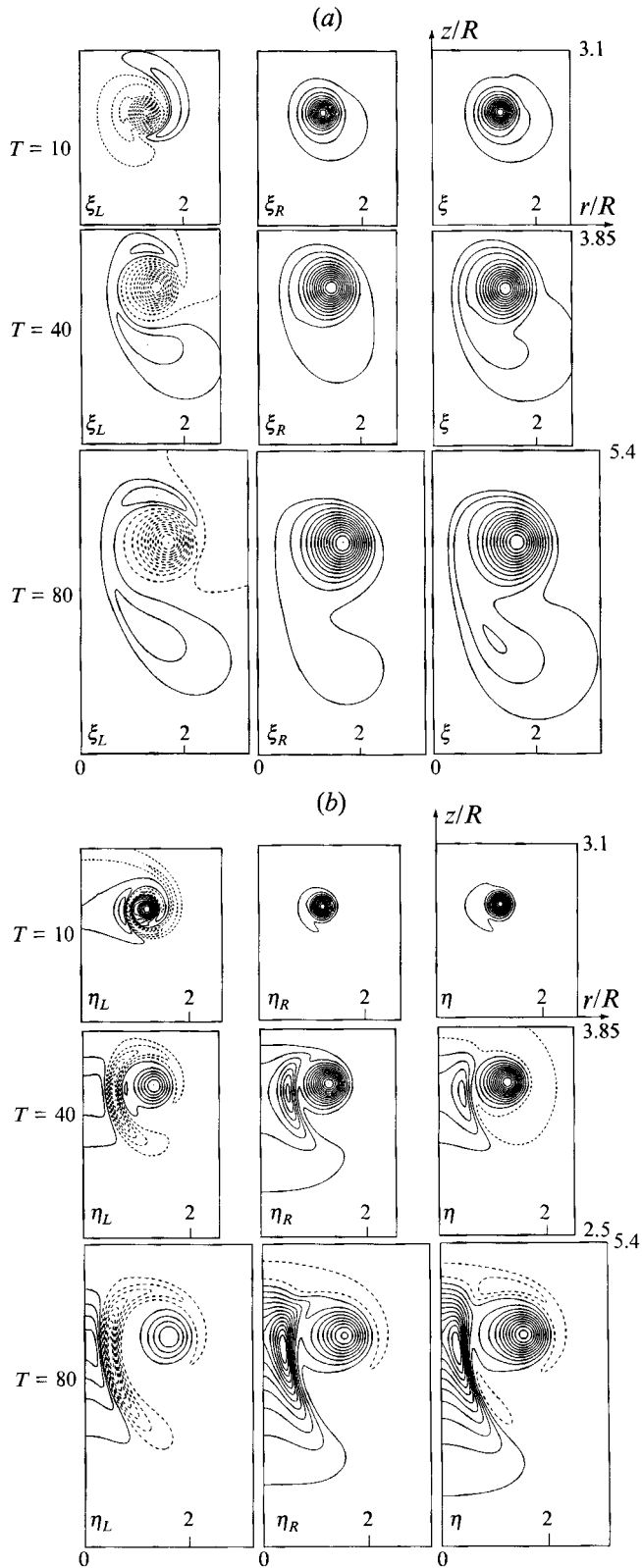
FIGURE 12. For caption see facing page.

studies (Melander & Hussain 1988, 1989; Kerr & Hussain 1989; Kida, Takoaka & Hussain 1989, 1991). In the terminology of magnetic reconnection (Greene 1988), the previous studies considered an X-point reconnection (i.e. the vorticity at the point of reconnection vanishes), while the configuration here is an O-point (i.e. reconnection along a circular vortex line); also see Melander & Hussain (1994). Similar reconnection would occur in the simulations of Grauer & Sideris (1991) and Pumir & Siggia (1992 a, b), had they considered the Navier–Stokes equations, rather than the Euler equations where reconnection is impossible.

5.5. *Evolution of polarized components*

The evolutions of polarized ξ and η are shown in figure 12(a, b) for case E ($\chi = 0$, $Re = 800$). Since ξ_L is zero initially and remains small throughout the evolution, the contours of ξ_R are very similar to those for ξ. Most of the generated ξ_L is negative and concentrated in the core. Thus, the total ξ in the core is smaller than ξ_R. As a result, the coupling term is reduced compared to that due to ξ_R alone. Therefore, the generation of ξ_L tends to reduce the η generation and hence further generation of η_L. Likewise, the η_R-contours are very similar to η-contours since η_L remains small throughout the evolution. The most interesting aspect of the polarized dynamics is the formation of left- and right-handed sheets outside the core; see η_L and η_R in figure 12(b). These sheets are formed in a spiral pattern next to the core ($T = 10$). Then they gradually move away from the core and towards the axis ($T = 80$). In the process they increase in strength and establish the axial tail vortex. The two sheets in η_L are parallel and separated by approximately a third of the sheet thickness; η_R has a peak on the negative η_L sheet, but away from the negative η_L peak. This causes significant spatial variation of local polarization.

The evolutions of polarized ξ- and η-components for case D ($Re = 800$, $\chi = 0.5$) are shown in figure 14(a, b). The ξ-components evolve similarly to those in case E. However, the new vortex formed by reconnection is clearer at $T = 40$ and is well separated from the head at $T = 150$ due to the faster axial motion of the head. The head retains its original polarity, but the tail vortex has right-handed polarity near the axis and left-handed away from the axis. The evolution of η also shows an additional feature not see in case E. Namely, the η_L and η_R sheets both collapse onto the axis (figure 14b). The η_R sheet reaches the axis first followed shortly afterwards by the η_L sheet. Thereby the vortex dynamics of the axial vortex becomes qualitatively similar to the core dynamics described in Melander & Hussain (1993), except for the additional effect of having a nearby vortex ring.

5.6. *Decay of circulation*

The annihilation of circulation (Γ) is controlled by the η-distribution on the axis (28). Since fully and partially polarized rings feature generation of η on the axis as part of the axial vortex, Γ should decay faster than in the unpolarized ring. The evolution of the decay constant $-D_a \equiv (\mathrm{d}\Gamma/\mathrm{d}t)/\Gamma$ (figure 15a, b) shows that this is indeed the case. At any given instant maximum D_a occurs for a different value of χ. Initially $\chi = 0$ has maximum D_a, but later it is maximum for higher values of χ. In the large time limit, D_a vanishes as all cases lead to a Stokes ring in their final decay (Phillips 1956).

Two competing effects determine D_a: (i) generation of η on the axis by the coupling term, and (ii) the length of the tail as controlled by the axial motion of the head. The first increases with increasing degree of polarization while the second decreases. Hence, we expect the D_a to be maximum for an intermediate χ as soon as a tail forms. D_a is maximum somewhere in the range $0.125 < \chi < 0.5$ for the low-Re cases (figure 15b). A
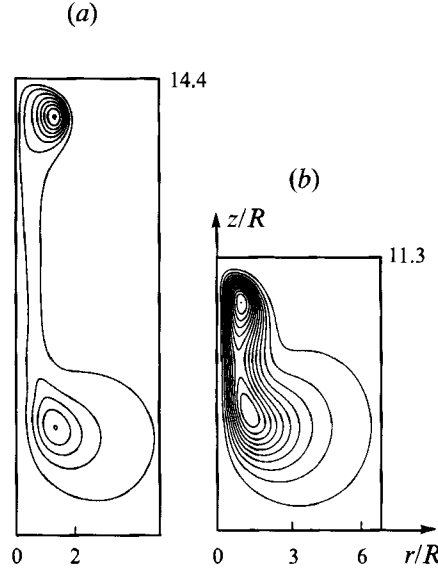
(a)

(b)

FIGURE 13. Breakup of vortex surfaces (ξ-contours). (a) Case C ($\chi = 0.75$, $Re = 800$) at $T = 150$ (only a part of the domain is shown). (b) Case F ($\chi = 0.75$, $Re = 150$) at $T = 96$.

similar trend is observed in the high-Re cases (figure 15a). Note that D_a ($\chi = 0.5$) is much higher in the high-Re case than in the low-Re case. This is because the axial motion of the head and η-generation control the viscous annihilation.

5.7. *Motion of the head*

Near the axis ω_θ is small, $\omega_\theta \propto r$. Knowing that the tail is close to the axis, we conclude that ω_θ is mainly associated with the head. The location of the head in the meridional plane is therefore well described by

$$(r_c, z_c) = \frac{1}{\Gamma} \int (r, z) \, \omega_\theta \, \mathrm{d}A. \tag{29}$$

The advance of the head is traced in figure 16(a, b). At all times, the axial motion of the head is in the upward direction. The radial motion is, however, more subtle. Early in the evolution, when the tail forms on the axis, r_c decreases slightly. Later when the annihilation of ω_θ sets in, the head begins its outward journey. In the final viscous decay of the rings, r_c will increase as $(4\nu t)^{\frac{1}{2}}$. This explains why r_c is farthest from the axis in the low-Re simulations.

The motion of the head has an interesting dependence on the initial degree of polarization $(1 - \chi)$. As expected, the axial ascent slows down considerably with increasing polarization. However, the radial motion again holds a surprise, for one would at first assume that the centrifugal force associated with a higher swirl content results in a more rapid radial motion. Figure 16(b) tells a different story. Namely, that the partially polarized ring (D) has the fastest radial motion. The reason is that the annihilation of ω_θ is highest in case D because of its very long tail.
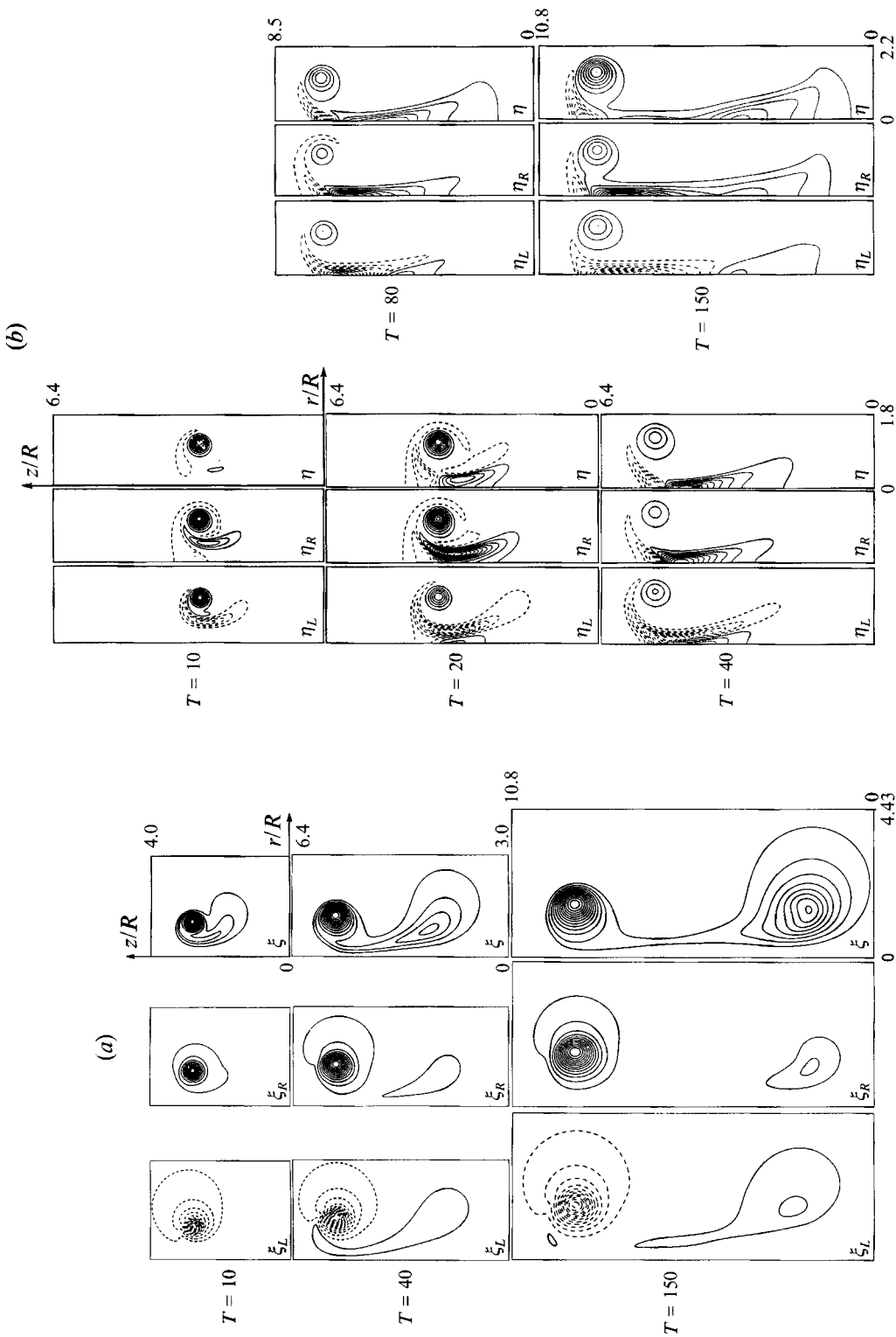
FIGURE 14. Evolution of polarized components for case D ($\chi = 0.5$, $Re = 800$). Only a part of the domain is shown; the (min., max.) values are: (a) $T = 10$, ξ_L (−0.92, 0.036), ξ_R (0.125, 1.74), ξ (0.059, 0.832); $T = 40$, ξ_L (−0.6, 0.059), ξ_R (0.029, 0.4); $T = 150$, ξ_L (−0.3, 0.042), ξ_R (−0.002, 0.439), ξ (0.012, 0.133). (b) $T = 10$, η_L (−0.346, 0.776), η_R (−0.143, 1.483), η (−0.205, 2.258); $T = 20$, η_L (−0.55, 0.489), η_R (−0.151, 0.908), η_L (−0.285, 1.297); $T = 40$, η_L (−0.864, 0.314), η_R (−0.838, 1.869), η (−1.28, 1.85); $T = 80$ η_L (−0.532, 0.113), η_R (−0.364, 0.637), η (−0.625, 0.358); $T = 150$, η_L (−0.161, 0.047), η_R (−0.061, 0.182), η (−0.109, 0.114). In each frame, the contour levels are equispaced.
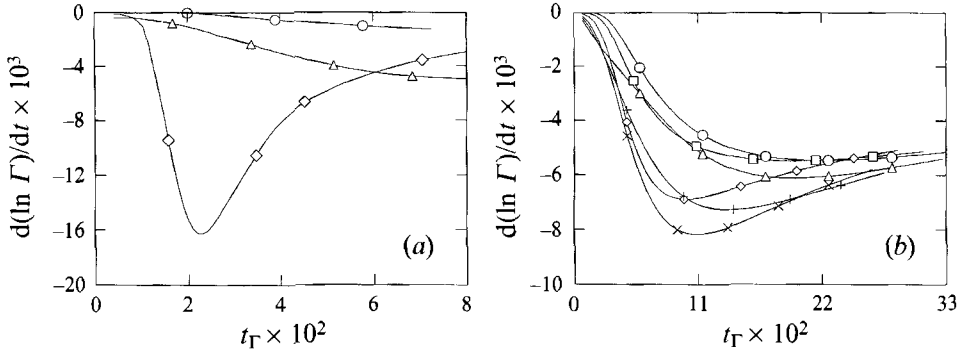
FIGURE 15. (a) Evolution of $-D_a \equiv (d\Gamma/dt)/\Gamma$ for $Re = 800$ cases A ($\bigcirc$, $\chi = 1.0$), D ($\Diamond$, $\chi = 0.5$) and E ($\triangle$, $\chi = 0$). (b) Evolution of $-D_a$ for $Re = 150$, case B ($\bigcirc$, $\chi = 1.0$), F ($\square$, $\chi = 0.75$), G ($\Diamond$, $\chi = 0.5$), H ($\times$, $\chi = 0.25$), I ($+$, $\chi = 0.125$), J ($\triangle$, $\chi = 0$).
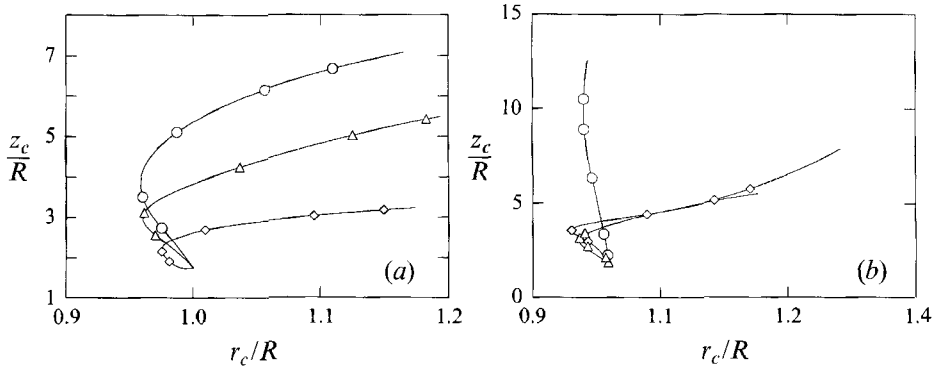

FIGURE 16. (a) Centroid locations (z_c and x_c defined in (29)) at $T = 10, 20, 50, 80, 100$ for $Re = 150$ cases B ($\bigcirc$, $\chi = 1.0$), G ($\triangle$, $\chi = 0.5$), J ($\Diamond$, $\chi = 0$). (b) The same for $Re = 800$ cases A ($\bigcirc$, $\chi = 1.0$), D ($\Diamond$, $\chi = 0.5$) and E ($\triangle$, $\chi = 0$).

6. Analysis of propagation velocity

6.1. *Force-balance argument*

The effect of tangential flow in a curved vortex filament is reported in the literature (Saffman 1970; Widnall *et al.* 1971; Moore & Saffman 1972). All predict reduction of the propagation velocity U_p. Moore & Saffman calculate U_p by balancing forces acting on an element of the filament. Two forces act away from the filament's centre of curvature; namely, the centrifugal force due to the tangential flow and the Kutta lift force. A balance is maintained through inward-acting forces, which are independent of both U_p and the tangential flow. Consequently, the Kutta lift force must be smaller in the presence of tangential flow. Since the Kutta lift force is proportional to U_p, they conclude that U_p must be smaller. Unfortunately, this argument only holds for thin rings ($a/R \ll 1$) as it is based on asymptotics valid to $O((a/R)^2)$.

6.2. *Propagation of Saffman's vortex centroid*

In a study of viscous vortex rings, Saffman (1970) defined the vortex centroid of a general three-dimensional vortex as

$$X = \frac{1}{2}\int \frac{r \times \omega \cdot I}{I^2} r\,dV, \quad U = \frac{dX}{dt} = \frac{1}{2}\int \frac{(r \times \partial\omega/\partial t)\cdot I}{I^2} r\,dV, \tag{30}$$
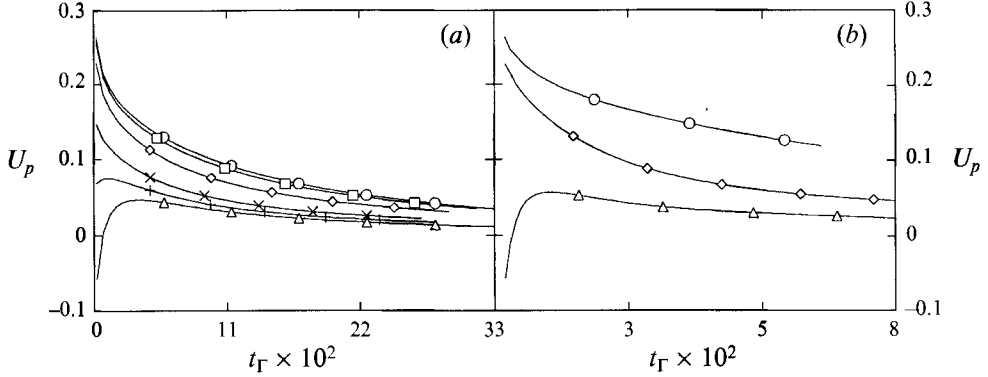
FIGURE 17. (a) Evolution of propagation velocity defined in (31) for $Re = 150$ cases B ($\bigcirc$, $\chi = 1.0$), F ($\square$, $\chi = 0.75$), G ($\diamondsuit$, $\chi = 0.5$), H ($\times$, $\chi = 0.25$), I ($+$, $\chi = 0.125$), J ($\triangle$, $\chi = 0$). (b) The same for $Re = 800$ cases A ($\bigcirc$, $\chi = 1.0$), D ($\diamondsuit$, $\chi = 0.5$) and E ($\triangle$, $\chi = 0$).

Case	$\int u_\theta^2 r\,dA$	From (33)	From (31)	Error (%)
B	0.0	0.2581	0.2624	1.64
F	0.0431	0.2517	0.2559	1.64
G	0.2276	0.2240	0.2292	2.27
H	0.7600	0.1443	0.1473	2.04
I	1.2771	0.0669	0.0690	3.04
J	2.1110	-0.0579	-0.0573	-1.05

TABLE 2. Comparison of estimated and observed U_p for $Re = 150$. Per cent error is defined as [100 (col. 4–col. 3)/(col. 4)]; $(4\nu t)^{\frac{1}{2}}$ in (33) is estimated from equating coefficient of (13) with that of Oseen solution, i.e. $1/(4\nu t)^{\frac{1}{2}} = (\omega_o \pi/\Gamma)^{\frac{1}{2}}$.

where $I = \frac{1}{2}\rho \int r \times \omega\,dV$ is linear impulse and integration is over the infinite volume. In our case V is the (finite) computational domain. Since I is conserved in the sufficiently large domain used here, the basic assumption in derivation of this formula is met. For the axisymmetric case, (30) reduces to

$$U_p = \frac{\pi}{I} \int [\nabla \times (\boldsymbol{u} \times \boldsymbol{\omega})]_\theta\, r^2\, z\,dr\,dz \tag{31}$$

$$= \frac{\pi}{I} \int\int \left[-\frac{\partial}{\partial z}(u_z\,\omega_\theta) - \frac{\partial}{\partial r}(u_r\,\omega_\theta) + \frac{\partial}{\partial z}\left(\frac{u_\theta^2}{r}\right)\right] r^2\, z\,dr\,dz$$

$$= U_{unpolarized} + \frac{\pi}{I} \int \frac{\partial}{\partial z}\left(\frac{\xi^2}{r^4}\right) r^3\, z\,dr\,dz. \tag{32}$$

The first two terms in the integrand are identical for rings with and without swirl. The third term is unique to rings with swirl; note that it is exactly the coupling term discussed in §3. Following Saffman's analysis for thin viscous rings with swirl, we obtain

$$U_p = \frac{\Gamma}{4\pi R}\left\{ \log\frac{8R}{(4\nu t)^{\frac{1}{2}}} - 0.558 + O\left[\left(\frac{\nu t}{R^2}\right)^{\frac{1}{2}} \log\frac{\nu t}{R^2}\right]\right\} - \frac{1}{\Gamma R^2}\int r u_\theta^2\,dr\,dz. \tag{33}$$

Since a closed-form solution of $u_\theta(r, t)$ is not known, we compared this prediction at the initial instant with U_p from (31). This comparison, shown in table 2, indicates good agreement for all χ.
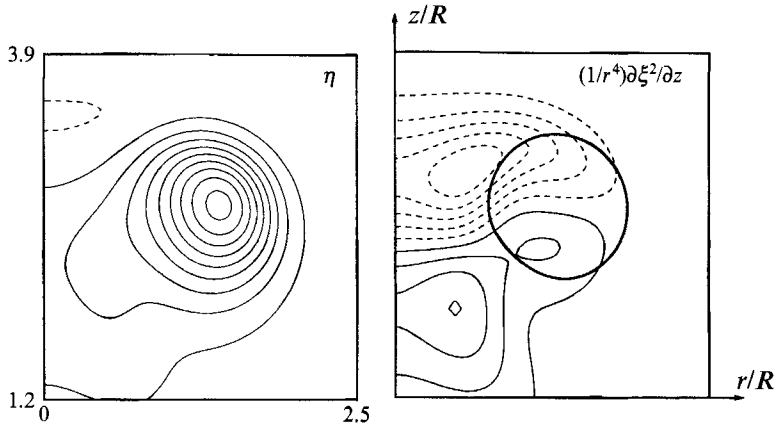
FIGURE 18. η and coupling term at $T = 10$ for case G ($\chi = 0.5$, $Re = 150$); contour levels (min., max., increment) are: η (-0.02, 0.45, 0.05), coupling term (-0.02, 0.016, 0.0045); the thick line on the coupling-term contours is $\eta = 0.2$. Only a part of the domain is shown.

The time evolution of U_p from (31) is shown in figure 17 (a, b). The trends are similar for both Re values. As χ decreases, U_p decreases since the effect of swirl increases, and for $\chi = 0$, negative U_p is observed initially! This is not inconsistent with the positive linear impulse since the ring (say, located at the peak ω_θ) still moves forward, but the *centroid* moves backwards due to large material generation of η in the back half of the vortex (discussed in §3).

6.3. *Coupling between meridional flow and swirl*

To predict U_p for rings with swirl, force balance arguments are tractable only for thin rings, making prediction for thick rings difficult. Our explanation of U_p reduction in rings with swirl due to generation of η (and hence ω_θ) at the back, i.e. opposite to the direction of self-induced ring motion and destruction of η at the ring front is supported by a plot of the coupling term and η in figure 18. The ring would move in the positive z-direction by self-induction. The positive and negative contours of the coupling term in the lower and upper halves of the η-distribution denote η-generation and destruction, respectively. As discussed in §3, the coupling term is higher for higher degree of polarization. Thus, with decreasing χ, generation/destruction of η due to the coupling term becomes higher, causing a larger decrease in U_p.

Another feature of these contours is that there is generation of η near the axis. This implies that for rings with swirl, η appears near the axis not only due to diffusion and advection, but also because of generation there. Since near the axis $u_\theta \sim r$, this gives $\xi^2 \sim r^4$ and therefore the coupling term $(1/r^4) \partial(\xi^2)/\partial z \sim O(1)$ on the axis. Recall that η on the axis leads to circulation decay; faster circulation decay reduces the self-induced velocity of the ring, as is clear from the slower axial motion of low-Re cases in figure 16 (a, b).

6.4. *Hill's spherical vortex with swirl*

Shariff & Leonard (1992) mention that, contrary to thin rings, Hill's spherical vortex would move faster when possessing weak swirl: 'The force balance argument does not apply for such a thick core and the speed of translation of Hill's vortices with *small* swirl is actually larger than in the swirl-free case' (emphasis is ours). Material generation of η in the back half of the core should, however, cause a reduction of U_p for polarized rings of all a/R, including Hill's spherical vortex, contrary to Shariff &
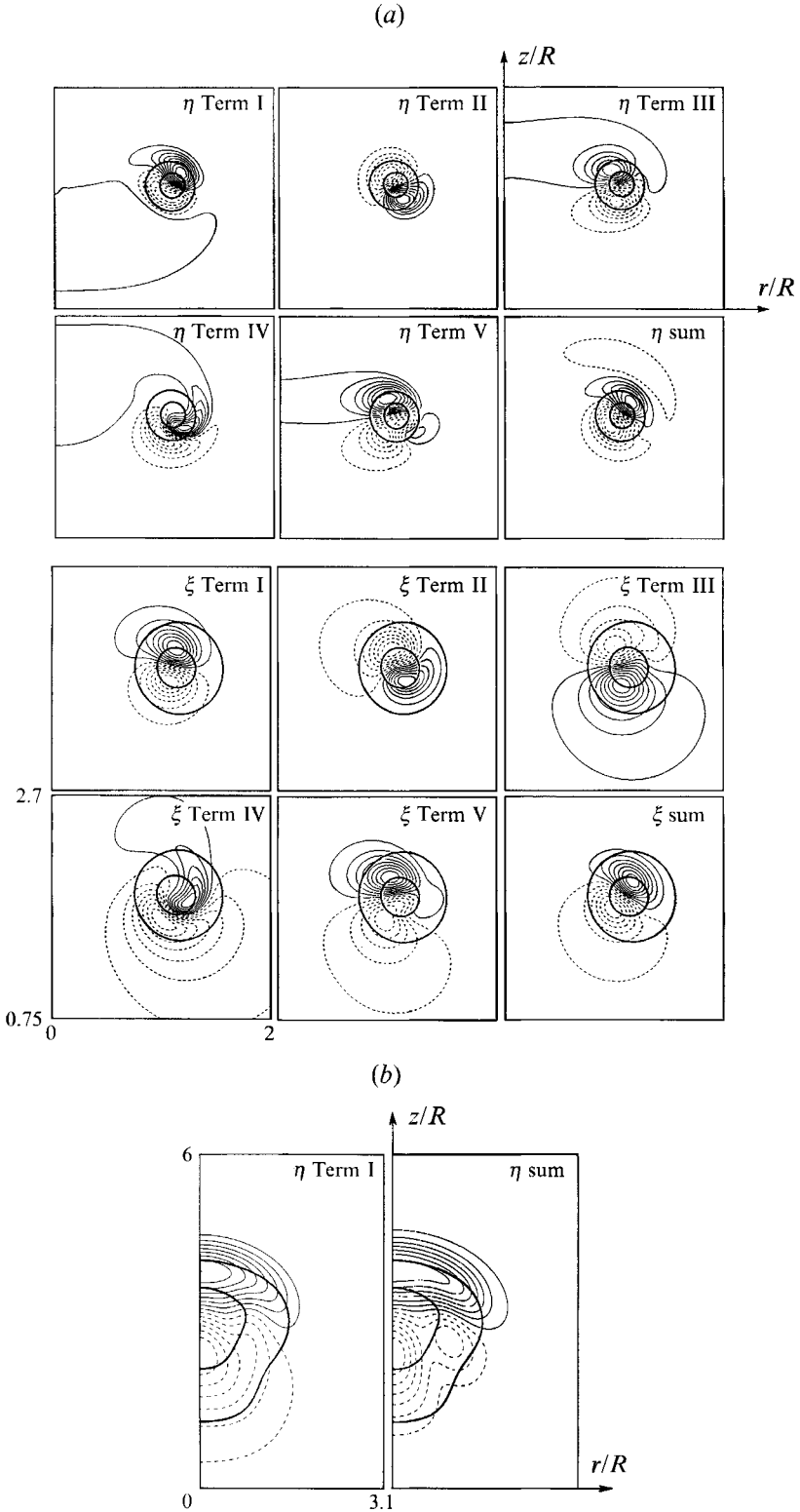
(*a*)

(*b*)

FIGURE 19. For caption see facing page.

Leonard's claim. Numerical results (not shown here) also support our argument. To further check our claim we analyse Moffatt's (1969) solution of Hill's spherical vortex with swirl. In spherical coordinates, the stream function is

$$\psi = R^2 \sin^2 \theta \left[\frac{\lambda}{\alpha^2} + A \left(\frac{a}{R} \right)^{\frac{3}{2}} J_{\frac{3}{2}}(\alpha R) \right], \tag{34}$$

where J is the Bessel function of first kind, α is a swirl parameter, A is a constant, a is the radius of the vortex, and λ is given as $\omega_\theta = \lambda r$ for the zero-swirl case. In the limit $\alpha \to 0$, ψ is exactly that for Hill's vortex without swirl. Moffatt showed that matching this solution with the irrotational flow for $R > a$ requires that $\lambda/\alpha^2 = -AJ_{\frac{3}{2}}(\alpha a)$ and $U = -\frac{2}{3}\alpha a A J_{\frac{3}{2}}(\alpha a)$, where U is the speed of vortex propagation relative to the fluid at infinity (i.e. U_p). Thus,

$$\psi = \frac{3UR^2 \sin^2 \theta}{\alpha a} \frac{R^2 \left(-\cos(\alpha a) + \dfrac{\sin(\alpha a)}{\alpha a} \right) - a^2 \left(-\cos(\alpha R) + \dfrac{\sin(\alpha R)}{\alpha R} \right)}{2R^2 \left(\dfrac{-3\cos(\alpha a)}{\alpha a} - \sin(\alpha a) + \dfrac{3\sin(\alpha a)}{\alpha^2 a^2} \right)}, \tag{35}$$

and

$$\omega_\theta = \frac{1}{R^2} \frac{\partial}{\partial R} \left[R^2 \frac{\partial}{\partial R} \left(\frac{\psi}{R \sin \theta} \right) \right] + \frac{1}{R^2} \frac{\partial}{\partial \theta} \left[\frac{1}{\sin \theta} \frac{\partial}{\partial \theta} \left(\frac{\psi}{R} \right) \right]$$

$$= \frac{3aU \sin \theta (-R\alpha \cos(\alpha R) + \sin(\alpha R))}{2R^2 \left(-3 \dfrac{\cos(\alpha a)}{\alpha a} - \sin(\alpha a) + 3 \dfrac{\sin(\alpha a)}{\alpha^2 a^2} \right)}. \tag{36}$$

For small swirl, $\alpha \ll (1/a)$, expansion yields

$$\omega_\theta \approx \frac{45}{2} U \sin \theta \left(\frac{R}{a^2(1 - \frac{1}{8}\alpha^2 a^2)} \right) \left(\frac{1}{3} - \frac{\alpha^2 R^2}{30} \right). \tag{37}$$

Therefore, the circulation Γ for this vortex is

$$\Gamma = \frac{45U}{2a^2(1 - \frac{1}{8}\alpha^2 a^2)} \int_{R=0}^{a} \int_{\theta=0}^{\pi} \left(\frac{R}{3} - \frac{\alpha^2 R^3}{30} \right) R \sin \theta \, d\theta \, dR. \tag{38}$$

Thus, for Hill's vortices with the same Γ, we obtain

$$U = \frac{2}{45} \Gamma a^2 \left(1 - \frac{\alpha^2 a^2}{14} \right) \frac{1}{\frac{2}{9}a^3(1 - \frac{3}{50}\alpha^2 a^2)} \approx \frac{\Gamma}{5a} \left(1 - \frac{2}{175}\alpha^2 a^2 \right). \tag{39}$$

Clearly, the translation velocity of Hill's vortex also decreases. Note that for the case of zero swirl ($\alpha = 0$), we recover the translation velocity for the swirl-free Hill's vortex given in Batchelor (1967, p. 526) by replacing $\Gamma = \frac{2}{3}\lambda a^3$. Surprisingly, (39) also appears in the little-known, but comprehensive, paper on vortex rings with swirl by Hicks (1899), which was unknown to the authors until after the submission of the paper. A

FIGURE 19. (*a*) Terms of polarized evolution equation (25) for ξ and η for $Re = 150$ case J ($\chi = 0$) at $T = 2$; the (min., max.) values are: η Term I ($-0.307, 0.416$), η Term II ($-0.14, 0.167$), η Term III ($-0.141, 0.113$), η Term IV ($-0.029, 0.03$), η Term V ($-0.036, 0.052$), Sum of η Terms I–V ($-0.425, 0.41$), ξ Term I ($-0.413, 0.462$), ξ Term II ($-0.144, 0.1386$), ξ Term III ($-0.078, 0.1176$), ξ Term IV ($-0.021, 0.017$), ξ Term V ($-0.018, 0.03$), Sum of ξ Terms I–V ($-0.266, 0.34$); the thick lines on contours of η-equation terms are η contours 0.05 and 0.15, the thick lines on contours of ξ-equation terms are ξ contours 0.05, and 0.15. (*b*) Term I and sum of Terms I–V in η (25) for case J ($Re = 150$, $\chi = 0$) at $T = 86$; the peak values are: Term I ($-0.00072, 0.00088$), Sum ($-0.000696, 0.000716$); thick lines are η-contours.
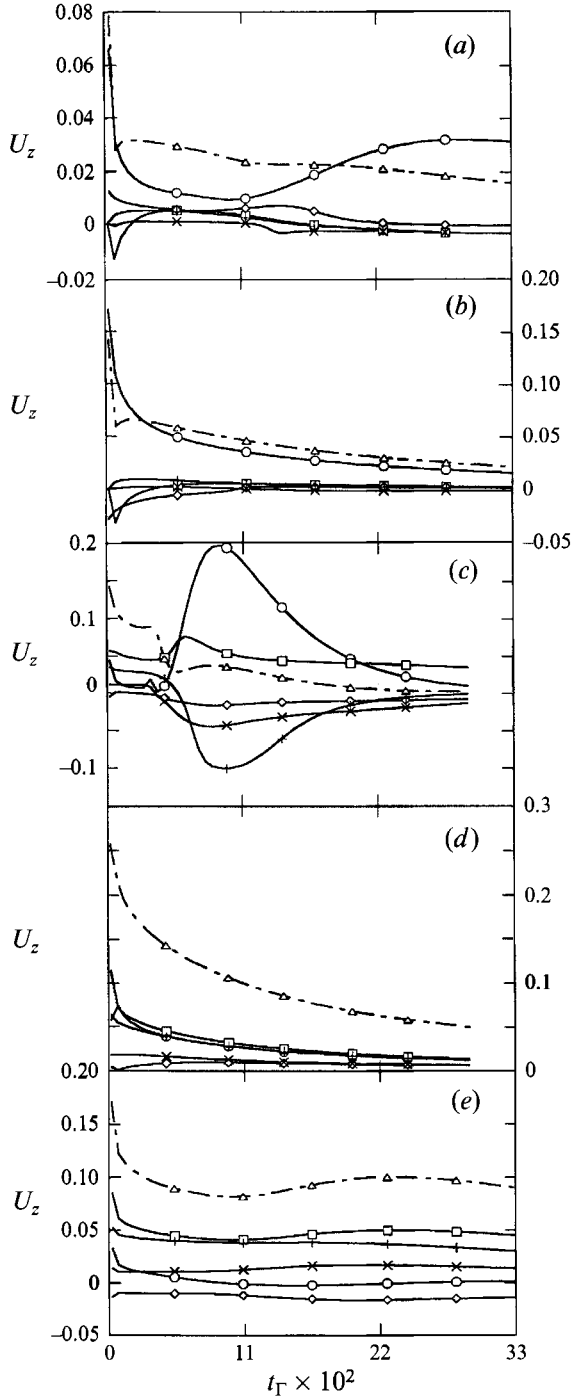
FIGURE 20. Evolution of axial dipole moment of Terms I ($\bigcirc$), II ($\square$), III ($\lozenge$), IV ($\times$), V ($+$), and their sum ($\triangle$) in (25): $U_z = U\hat{n}_z$, where U is defined in (40c) and n_z is the z-component of n defined in (40b). (a) η_R for case J ($\chi = 0$, $Re = 150$); (b) ξ_R, for case J; (c) η_R, for case G ($\chi = 0.5$, $Re = 150$); (d) ξ_R, for case G; (e) η_R, for case B ($\chi = 1.0$, $Re = 150$).
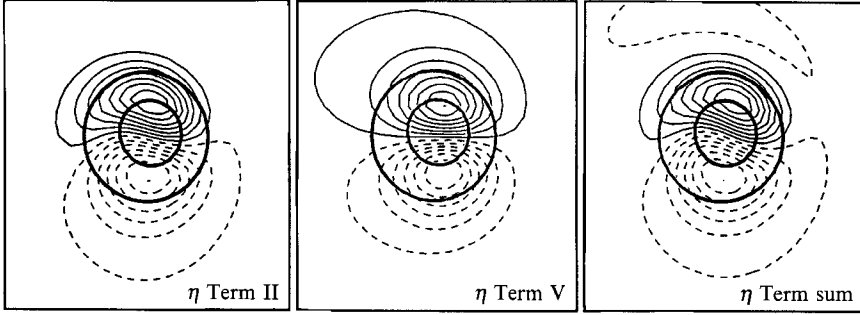
FIGURE 21. Terms II, V and sum of Terms I–V in (25) for case G ($\chi = 0.5$, $Re = 150$) at $T = 2$; the peak values (min., max.) are: Term II (-0.35, 0.44), Term V (-0.188, 0.208), Sum (-0.723, 0.94); in each frame, the contour levels are equispaced; thick lines are the η-contours.

referee pointed out that Shariff & Leonard considered rings with the same λ value, which is inappropriate for comparison between rings with the same Γ value; our simulations as well as the theory assume the same Γ value.

6.5. *Interaction between polarized components*

We find another explanation for U_p reduction by analysing the terms in (25). Figure 19(a) shows the terms I–V as well as their sum for the right-polarized case J at an early time in the evolution. As expected, the self-evolution (I) is dominant. However, advection by left-handed velocity (II) and transfer to the left-handed field (III) are also significant. We make an important observation here: namely, that all terms exhibit a '*dipole-like*' structure when plotted in the meridional plane. This dipole-like structure is seen throughout the evolution. As an illustration, we show the contours at $T = 86$ in figure 19(b).

The dipole-like structure helps us extract the propagation velocity associated with each term in (25). To see this, consider the distribution, for example a Gaussian, of a scalar quantity f with a single peak in the (r, z)-plane. Suppose f is steady in a frame moving with an unknown velocity U, then $\partial f/\partial t$ is a dipole-like structure in the (r, z)-plane. Moreover, $\partial f/\partial t + U \cdot \nabla f = 0$. Knowledge of $\partial f/\partial t$ and f readily allows us to find U. By fitting our data (e.g. with ξ_R as f and term I as $\partial f/\partial t$) to this simple advection equation we obtain the propagation velocity associated with each term in (25). The fitting procedure is described in the next paragraph.

In order to focus on the main peak, which is associated with the head, we weight the terms by f^4. After adjusting for the mean increase or decrease in f, we calculate a unit vector $\hat{n}$ and a magnitude U for the propagation velocity. The explicit fitting is then given by

$$M = \int f^4 (\partial f/\partial t) \, \mathrm{d}A; \quad n = \int \left(\frac{\partial f}{\partial t} - \frac{M}{\int f^4 \, \mathrm{d}A} \right) (r, z) f^4 \, \mathrm{d}A, \qquad (40\,a, b)$$

$$U^2 = \int f^8 \left(\frac{\partial f}{\partial t} - \frac{M}{\int f^4 \, \mathrm{d}A} \right)^2 \mathrm{d}A \bigg/ \int f^8 (\hat{n} \cdot \nabla f)^2 \, \mathrm{d}A, \qquad (40\,c)$$

where all integrals are over the entire meridional plane.

As an example of typical trends, we show in figure 20(a–d) the evolutions of the ξ- and η-terms for $Re = 150$ cases G ($\chi = 0.5$) and J ($\chi = 0$). Only the z-direction is included as this is the direction of ring motion. We find that the evolution of the fully polarized ring is dominated by term I for both ξ and η. However, for the partially-polarized case, term II is the most dominant η-term during most of the evolution, with
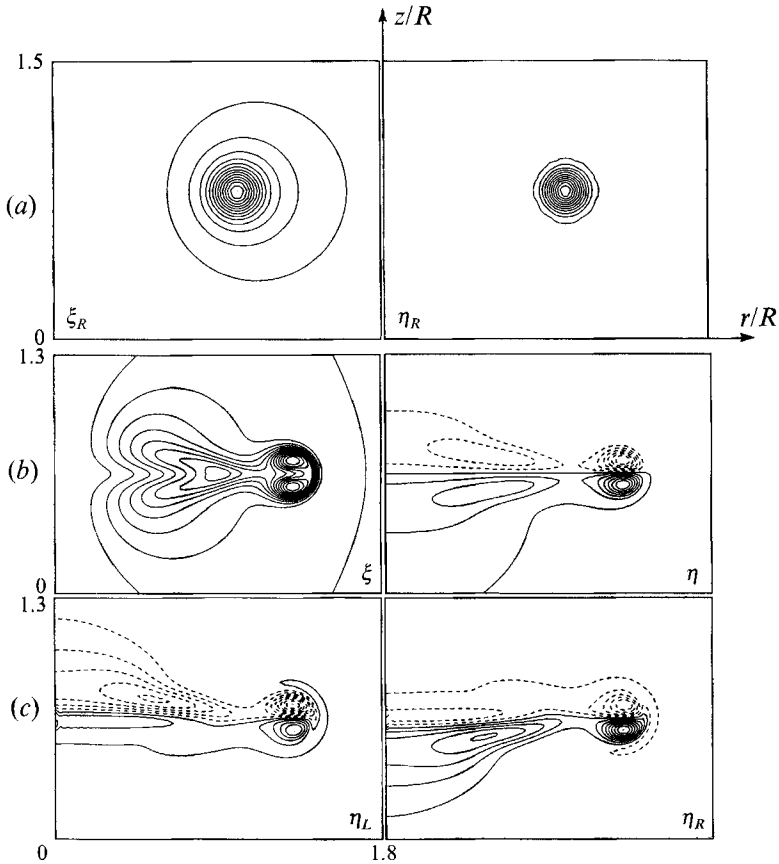
FIGURE 22. (a) ξ_R and ξ_L at $T = 0$ for the $\chi = -1.0$ case K, initially $\xi_L = \xi_R$, $\eta_L = -\eta_R$ and $\eta = 0$ for this case; the peak values (min., max.) are: ξ_R (0.17, 2.43), η_R (-0.96, 3.72). (b) ξ and η at $T = 32$ for the same case to show the generation of η due to the coupling term; the peak values are: ξ (0.038, 0.53), η (-0.129, 0.131). (c) η_L and η_R at $T = 32$ show that negative η in front is due to advection of η_L by η_R as expected from Term II of (25); the peak values are: η_L (-0.082, 0.049), η_R (-0.049, 0.082). Contour levels are equispaced in all.

terms I and V also being important at intermediate times. For the unpolarized case (only η-terms shown in figure 20 e), we find that terms II and V are the most important. Note that at early times, the sign of term II in the fully polarized case is opposite to that in the partially and unpolarized cases. This is consistent with the contours of this term shown in figure 19 (a) for the fully polarized case and figure 21 for the partially polarized case (contours for the unpolarized case are similar to those for partially-polarized cases and are not shown). Thus, we see that η_L generated by self-evolution of η_R causes a velocity field that opposes the forward motion of the ring. This is clear in the fully polarized case where η_L is initially zero. Therefore, all contributions to term II at later times are due to η_L generated by the coupling term. For the unpolarized and partially polarized cases, the effect of η_L present in the initial conditions is to move the ring forward, and that of the generated η_L is small. Even though η_L and hence left-handed velocity is small in the fully polarized case compared to the partially and unpolarized cases, its effect on advection of η_R is large because the velocity and *gradient* of η_R are more aligned than in the other cases.

From these results, we can provide some general results for constructing models for

the evolution of right-handed polarized rings. We find that term IV is always small and may be neglected. Term II is always important. Term I increases in importance with decreasing χ and term V decreases in importance. Term III is important only at low χ.

The two explanations we have presented for the slowing of polarized rings – one based on production of η due to the coupling term in (19) and the other on term II in (25) – are quite consistent, even equivalent. To illustrate this, we consider an academic case with $\chi = -1.0$ (such a configuration has also been studied by Grauer & Sideris 1991 with the different aim of finding a finite-time singularity in the Euler equations). In this case, initially $\omega_0 = 0$ and $\eta_L = -\eta_R$, $\xi_R = \xi_L$ (figure 22a). The coupling term in (19) generates negative η in front and positive η behind as shown in figure 22(b). Owing to mutual induction of the positive and negative η, the dipole moves radially outward. The axial motion of the negative and positive η (due to curvature) is equal and opposite, and therefore cancels. On the other hand, η_R and η_L would separate since they have self-induced velocities in opposite axial directions. But, owing to advection by the opposite handed velocity (term II in (25)), they separate in a direction opposite to that of self-evolution alone. As a result, we see negative η in front (corresponding to η_L) and positive η behind (corresponding to η_R) in figure 22, as also inferred from the coupling term in (19). Therefore, the generation of opposite-signed η in the upper and lower halves of the core due to the coupling term in (19) is equivalent to separation of polarized components due to advection by the component of opposite polarity. Motion in a direction opposite to that of self-advection due to the presence of opposite polarity was also observed for wave motion on a vortex of non-uniform cross-section (Melander & Hussain 1993). Further, note that dipole formation due to the coupling term causes the radially outward motion. This effect, also present in rings, increases with decreasing χ.

7. Concluding remarks

Motivated by our finding that most vortical structure in transitional and turbulent flows are polarized, we have developed a new algorithm for solving the vorticity transport equation, using divergence-free eigenfunctions of the curl operator in an axisymmetric geometry. This algorithm is validated by comparing results obtained with independent codes. Since ξ and η are natural variables for analysing axisymmetric vortical flows, we also derive evolution equations for polarized components of these variables.

As a first step in understanding the dynamics of polarized vortical structures, we have investigated the evolution of perhaps the simplest isolated polarized structure, namely, an axisymmetric ring. We find that polarization is a persistent feature of such structures. A polarized ring develops a head–tail structure, where the head is a vortex ring, but in contrast to unpolarized rings, the tail is an axial vortex. Such a columnar tail is a characteristic feature of polarized vortices and leads to a complicated vortex line geometry. Unlike in unpolarized rings, most Γ-annihilation occurs in the tail. The tail increases in strength with $(1 - \chi)$ and causes faster circulation decay. However, Γ-annihilation with increasing polarization is non-monotonic: the maximum $|d\Gamma/dt|$ occurs for $0.125 < \chi < 0.5$. This is because increased polarization also reduces the length of the tail, thus diminishing the effect of polarization at higher values.

As predicted by previous studies of vortex filaments with axial flow, we find that a ring propagates at a slower rate if polarized. The ring propagation is analysed, and we provide two equivalent vortex-dynamics-based explanations – one in terms of the coupling between the meridional flow and swirl, and the other in terms of the evolution

of polarized components – for the observed decrease in U_p with increasing initial polarization (i.e. swirl). Unlike force-balance arguments, which apply to thin rings only, these explanations are also valid for small ratios of ring to core radii. Also, contrary to a recent claim by Shariff & Leonard (1992), these explanations clearly suggest slowing down of thick rings with any amount of swirl; we also derive analytically such a reduction in U_p for Hill's spherical vortex with weak swirl.

The axisymmetric geometry allows us simple access to axisymmetric vortex surfaces, which reveal a new type of vortex reconnection distinct from that previously studied in an antiparallel vortex tube configuration. In the present case, the reconnecting vortex lines belong to the same vortical structure, and the vortex line configuration in the reconnection region is O-type with locally parallel lines, unlike the X-type with antiparallel vortex lines (Greene 1988). Interestingly, these topological changes are not evident in $|\omega|$-plots, which erroneously suggest reconnection near the head instead of at the lower region of the tail where it actually occurs. In a general three-dimensional case, one must therefore be very careful in identifying vortex reconnection based on $|\omega|$ surface plots. This study also illustrates that reconnection occurs not only in large-scale vortical structures; topological changes are observed in the tail region, thereby suggesting that small scales of a turbulent flow should also be analysed carefully in order to accurately ascertain the significance of vortex reconnection. This point emphasizes the value of studying the details of reconnection mechanism by DNS (at low Re), such an analysis having been criticized as irrelevant for turbulent flows. The axial tail vortex develops high gradients of vorticity, demonstrating the direct generation of small scales (hence cascade) by the evolution of an isolated large-scale (polarized) coherent structure.

Even though the overall polarization level (defined by the amounts of right- or left-handed energy, enstrophy and helicity) remains constant, significant variations in the local ratio of left- and right-handed vorticity components develop. The head maintains its initial polarization, but the tail develops substantial polarization variations due to relative axial shift of left- and right-handed vorticity components. The self-induced motion of polarized components in the head is in the azimuthal direction, so that separation is prevented by the imposed axisymmetry. In the tail, however, differential axial motion of the polarized components leads to significant spatial variation of polarization. These observations, combined with our earlier studies mentioned in §1, suggest that without constraining symmetries, the mechanisms leading to spatial polarization variations are strong and that the nonlinear generation of opposite polarity is weak. The relative importance of different mechanisms (i.e. the various terms in (25)) depends on χ and also changes in time.

The present study is but the first step in exploring polarized vorticity dynamics. In addition to axisymmetric ring interactions, the effect of polarization on instability and transition phenomena when axisymmetry is not enforced in the numerical simulations may reveal phenomena of relevance to turbulent flow modelling. Since unpolarized structures tend to become polarized in general, the cascade and topology-changing mechanisms discussed here may occur frequently in turbulent flows. Idealization and further analysis of the configurations of polarized structures observed upon evolution of initially unpolarized flows will be useful in further developing a physical understanding of the dynamics of transitional and turbulent flows.

REFERENCES

BATCHELOR, G. K. 1967 *An Introduction to Fluid Dynamics.* Cambridge University Press.

GRAUER, R. & SIDERIS, T. C. 1991 Numerical computation of 3D incompressible ideal fluids with swirl. *Phys. Rev. Lett.* **67**, 3511–3514.

GREENE, J. M. 1988 Geometrical properties of three-dimensional reconnecting magnetic fields with nulls. *J. Geophys. Res.* **93**, 8583–8590.

HICKS, W. M. 1899 Researches in vortex motion – Part III. On spiral or gyrostatic vortex aggregates. *Phil. Trans. R. Soc. Lond.* A. **192**, 33–99.

KERR, R. & HUSSAIN, F. 1989 Simulation of vortex reconnection. *Physica* D **37**, 474–484.

KIDA, S., TAKOAKA, M. & HUSSAIN, F. 1989 Reconnection of two vortex rings. *Phys. Fluids* A **1**, 630–632.

KIDA, S., TAKOAKA, M. & HUSSAIN, F. 1991 Collision of two vortex rings. *J. Fluid Mech.* **230**, 583–646.

LAMBERT, J. D. 1983 *Computational Methods in Ordinary Differential Equations.* John Wiley.

LESIEUR, M. 1990 *Turbulence in Fluids*, 2nd Edn. Kluwer.

MAXWORTHY, T. 1972 The structure and stability of vortex rings. *J. Fluid Mech.* **51**, 15–32.

MELANDER, M. & HUSSAIN, F. 1988 Cut-and-connect of two antiparallel vortex tubes. *CTR Rep.* S-21, pp. 257–286.

MELANDER, M. & HUSSAIN, F. 1989 Cross-linking of two antiparallel vortex tubes. *Phys. Fluids* A **1**, 633–636.

MELANDER, M. & HUSSAIN, F. 1993 Polarized vorticity dynamics on a vortex column. *Phys. Fluids* A **5**, 1992–2003.

MELANDER, M. & HUSSAIN, F. 1994 Topological vortex dynamics in axisymmetric viscous flows. *J. Fluid Mech.* **260**, 57–80.

MELANDER, M., HUSSAIN, F. & BASU, A. 1991 Breakdown of a circular jet into turbulence. *Eighth Symp. on Turb. Shear Flows, Munich*, pp. 15.5.1–15.5.6.

MOFFATT, H. K. 1969 The degree of knottedness of tangled vortex lines. *J. Fluid Mech.* **35**, 117–129.

MOFFATT, H. K. 1988 Generalized vortex rings with and without swirl. *Fluid Dyn. Res.* **3**, 22–30.

MOORE, D. & SAFFMAN, P. 1972 The motion of a vortex filament with axial flow. *Phil. Trans. R. Soc. Lond.* A **272**, 403–429.

MOSES, H. 1971 Eigenfunctions of the curl operator, rotationally invariant Helmholtz theorem, and applications to electromagnetic theory and fluid mechanics. *SIAM J. Appl. Math.* **21**, 114–144.

NORBURY, J. 1973 A family of steady vortex rings. *J. Fluid Mech.* **57**, 417–431.

PHILLIPS, O. M. 1956 The final period of decay of non-homogeneous turbulence. *Proc. Camb. Phil. Soc.* **52**, 135–151.

PUMIR, A. & SIGGIA,. E. 1992a Development of singular solutions to the axisymmetric Euler equations. *Phys. Fluids* A **4**, 1472–1491.

PUMIR, A. & SIGGIA, E. 1992b Finite-time singularities in the axisymmetric three-dimension Euler equations. *Phys. Rev. Lett.* **68**, 1511–1514.

SAFFMAN, P. 1970 The velocity of viscous vortex rings. *Stud. Appl. Maths.* **49**, 371–380.

SHARIFF, K. & LEONARD, A. 1992 Vortex rings. *Ann. Rev. Fluid Mech.* **24**, 235–279.

SHARIFF, K., LEONARD, A., ZABUSKY, N. J. & FERZIGER, J. H. 1988 Acoustics and dynamics of coaxial interacting vortex rings. *Fluid Dyn. Res.* **3**, 337–343.

STANAWAY, S., CANTWELL, B. & SPALART, P. 1988 A numerical study of viscous vortex rings using a spectral method. *NASA TM* 101041.

TURKINGTON, B. 1989 Vortex rings with swirl: axisymmetric solutions of the Euler equations with nonzero helicity. *SIAM J. Math. Anal.* **20**, 57–73.

WIDNALL, S., BLISS, D. & ZALAY, A. 1971 Theoretical and experimental study of the stability of a vortex pair. In *Aircraft Wake Turbulence and its Detection*, pp. 305–329. Plenum.